

Harnessing omnipresent oscillator networks as computational resource

Thomas Geert de Jong¹ Hirofumi Notsu¹ Kohei Nakajima²

¹Kanazawa University ²University of Tokyo
{ tgdejong, notsu }@se.kanazawa-u.ac.jp,
k-nakajima@isi.imi.i.u-tokyo.ac.jp

February 10, 2025

Abstract: Nature is pervaded with oscillatory behavior. In networks of coupled oscillators patterns can arise when the system synchronizes to an external input. Hence, these networks provide processing and memory of input. We present a universal framework for harnessing oscillator networks as computational resource. This reservoir computing framework is introduced by the ubiquitous model for phase-locking, the Kuramoto model. We force the Kuramoto model by a nonlinear target-system, then after substituting the target-system with a trained feedback-loop it emulates the target-system. Our results are two-fold. Firstly, the trained network inherits performance properties of the Kuramoto model, where all-to-all coupling is performed in linear time with respect to the number of nodes and parameters for synchronization are abundant. Secondly, the learning capabilities of the oscillator network can be explained using Kuramoto model’s order parameter. This work provides the foundation for utilizing nature’s oscillator networks as a new class of information processing systems.

Keywords: Collective intelligence, universal reservoir computing, explainability of neural networks, learning bifurcations, generalized synchronization, oscillator networks.

1 Introduction

Oscillatory behaviour is foundational to the fabric of nature, ranging from pacemaker cells in the heart, to life-cycles of phytoplankton, to circadian rhythms, and to brainwaves [Win01]. Typically, the dynamics arising from these phenomena is the result of a network of oscillators. When coupled, even weakly, and under the right conditions the oscillators adjust their phases such that the oscillator network exhibits synchronous behaviour [Kur84]. Such synchronous behaviour can be sustained without central guiding mechanism. Moreover, if the network is sufficiently complex the system is robust to damage, adaptable to change and scales to different sizes [LBAJ23]. Additionally, biological networks that we find in nature are efficient from an energy and resource perspective compared to their artificial counterparts [Que24].

Networks are already ubiquitously used as a computational resource. In the last decade we have seen artificial neural networks outperforming state-of-the-art model driven approaches [LBH15, KT19, DVB⁺21, JEP⁺21, RDN⁺22]. These properties are attributed to having a network architecture that resembles the connectivity of biological neurons by synapses. However, at a fundamental level artificial networks perform operations differently to biological networks. Hence, to deploy biological networks as a computational resources we require a framework that takes into account the underlying biological dynamics.

We propose a framework for utilizing weakly coupled oscillatory networks as a computational resource to solve learning tasks such that the full system inherits properties of the coupled oscillators. In this Article we apply the framework to the ubiquitous model for phase-locking, the Kuramoto model [Kur75]. More specifically, in the Kuramoto model the oscillators have different natural frequencies which for suitable coupling start rotating with a common frequency, i.e. the oscillators *lock their phases*. When adding external forcing the Kuramoto model can synchronize to external input [AFG⁺08, CS08]. Hence, it provides processing and memory of the input. We will consider a pattern prediction task where the pattern is a trajectory on a chaotic attractor which is described by a bounded deterministic yet unpredictable motion [Lor63]. Chaotic attractors arise due to the geometry underlying the governing equations. Therefore,

their complexities are quantifiable which gives additional performance tests for learning tasks. Moreover, like oscillatory phenomenon, chaotic dynamics are ubiquitous in nature [PJSF04].

The computational capabilities of the Kuramoto model will be harnessed using the reservoir computing architecture [JH04]. The evolution of a reservoir computer is represented as a coupled network with a massive amount of nonlinear nodes called the *reservoir*. Reservoir computing provides one of the major frameworks for hardware that emulate neural networks referred to as neuromorphic devices [Nak20, TYH⁺19, Nak18]. Here the reservoir is given by coupled Kuramoto oscillators subject to a forcing term driven by the input. Then decoupling the system from the input by substituting the input with a feedback-loop the network reproduces the attractor. This input-decoupled system is commonly referred to as the closed system. Our results are

- Although the system describes an all-to-all coupling, simulations inherit Kuramoto’s linear time-complexity with respect to number of oscillators;
- The vast literature on Kuramoto models [Str00] can be used to explain the performance of the closed system. We use the so-called order parameter which averages the position of the oscillating components of the Kuramoto model and show that the time-series of the order parameter encodes the complex geometry of the attractor;
- The closed system is successful when a self-sustained synchronization is achieved. It is easy-to-configure in the sense that the hyper-parameters that lead to success are abundant. Additionally, for hyper-parameters that lead to failure we provide a simple test to identify oscillators that bar reproducing the attractor’s geometry.

2 Results

2.1 Background

The modern study of collective synchronization was initiated by Winfree [Win67]. He cast the problem as a population of interacting limit-cycle oscillators. This problem proved to be complicated. Winfree realized that its complexity would be reduced if the couplings are weak and the oscillators nearly identical. Kuramoto [Kur84] continued this approach by realizing that using averaging techniques [SVM07] the long-term dynamics are given by the universal form:

$$\frac{d\theta_k}{dt} = \omega_k + \sum_{j=1}^N \Gamma_{jk}(\theta_j - \theta_k), \quad 1 \leq k \leq N,$$

where $\theta_k(t) \in \mathbb{R}/2\pi\mathbb{Z} =: \mathbb{S}$ denotes the phase of the i th oscillator with $\omega_k \in \mathbb{R}$ its natural frequency and Γ_{jk} the interaction function. It will be useful to imagine that the oscillators $\theta = (\theta_1, \theta_2, \dots, \theta_N)$ all move on a common circle. We will focus on the Kuramoto model for which $\Gamma_{jk}(\theta_j - \theta_k) = \frac{K}{N} \sin(\theta_j - \theta_k)$ with $K \geq 0$ the coupling strength. Observe that this leads to an all-to-all coupling. Alternative Γ_{jk} for our framework are discussed in the Supplementary Information.

2.2 Kuramoto model as reservoir computer

The construction of our reservoir computer by Kuramoto model proceeds in three steps (Fig. 1). The first step is to introduce a forcing term in the Kuramoto model that allows for synchronization to an external input u (Fig. 1). We consider an input $u(t) = (u_1(t), u_2(t), \dots, u_M(t)) \in \mathbb{R}^M$. The input-driven Kuramoto equations are then given by

$$\frac{d\theta_k}{dt} = \omega_k + \underbrace{\frac{K}{N} \sum_{j=1}^N [\sin(\theta_j - \theta_k)]}_{\text{coupling}} + \underbrace{F \sin(cu_{v_k} - \theta_k)}_{\text{forcing}}, \quad 1 \leq k \leq N, \quad (1)$$

where ω_k will be sampled from $2\pi\mathcal{N}$ with \mathcal{N} denoting the normal distribution with mean 1 and standard deviation 1, v_k uniformly sampled from $\{1, 2, \dots, M\}$, and c the input scaling constant. The parameters $K, F \geq 0$ will be referred to as the coupling and forcing parameters, respectively. Equation (1) is inspired by the Forced Kuramoto equations considered in [Sak88, AFG⁺08, OA08, CS08].

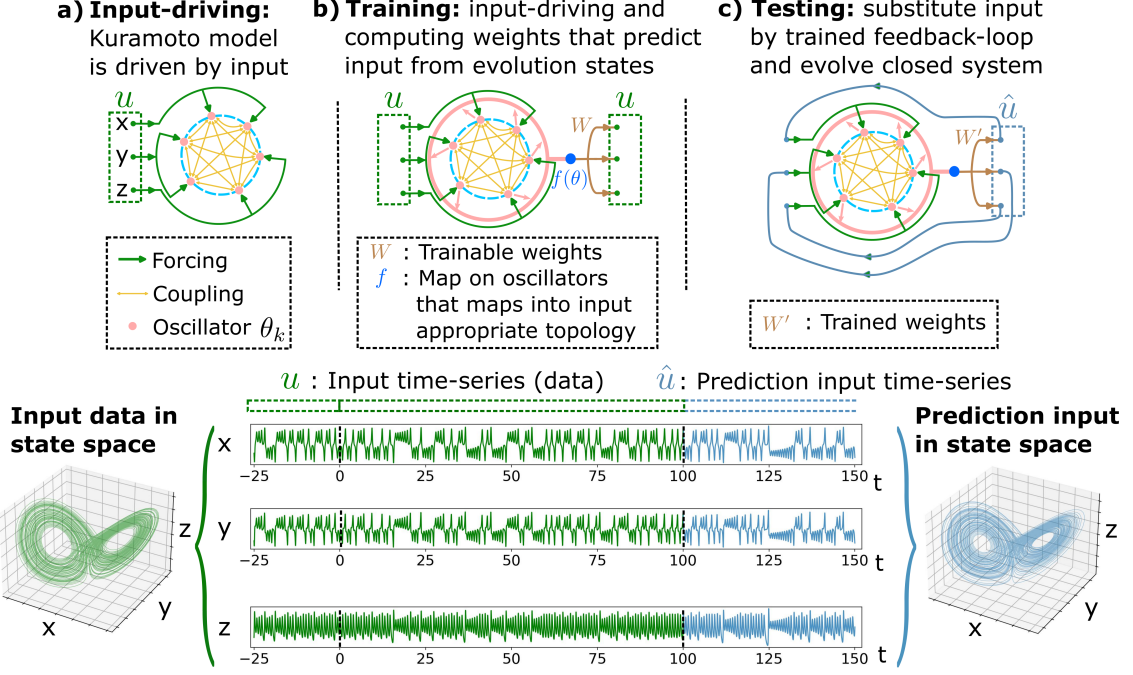


Figure 1: **Overview for constructing the Kuramoto reservoir:** After driving and training we obtain a closed system for testing.

The second step is to train a function g such that $g(\theta) \approx u$ (Fig. 1b). The aim is to use regression but as $\theta_k(t) \in \mathbb{S}$ and $u_j(t) \in \mathbb{R}$ we need an intermediate function which maps $\theta_k(t)$ to an appropriate topology. We define the N -dimensional torus \mathbb{T}^N as the Cartesian product over N sets of \mathbb{S} and consider the so-called read-out function $f : \mathbb{T}^N \rightarrow \mathbb{R}^{2N+1}$ given by $f(\theta) = [1, \sin(\theta), \sin^2(\theta)]$ with the first component generating the bias-terms. Alternative read-out functions are considered in the Supplementary Information. Driving Equation (1) for T time-steps we represent the resulting time series vectors for θ and u as an $N \times T$ -matrix Θ and an $M \times T$ -matrix U , respectively. We are then interested in determining

$$W' = \arg \min_W \|W \hat{f}(\Theta) - U\|_2^2 + \varepsilon \|W\|_2^2,$$

with $\hat{f} : \mathbb{T}^{N \times T} \rightarrow \mathbb{R}^{(2N+1) \times T}$ given by applying f on the components in the time-direction and where ε -term with $\varepsilon > 0$ acts as a regularization term which will improve robustness.

The final step (Fig. 1c) is to substitute u in Equation (1) by $W'f(\theta)$,

$$\frac{d\theta_k}{dt} = \omega_k + \frac{K}{N} \sum_{j=1}^N [\sin(\theta_j - \theta_k)] + F \sin(c[W'f(\theta)]_{v_k} - \theta_k). \quad (2)$$

We define $\hat{u} = W'f(\theta)$. Then, we observe that $\hat{u} \approx u$. In this Article \hat{u} will be referred to as the prediction. Since u has been decoupled from (2) this equation is typically referred to as the closed reservoir. It will be used for all the results in this Article. We refer to this reservoir as the Kuramoto reservoir but shall just refer to it as the reservoir when it is clear from the context.

Finally, we need to consider an input time series. We consider a trajectory $u = (x, y, z)$ on the Lorenz attractor which is obtained from

$$\begin{aligned} \frac{dx}{dt} &= \sigma(y - x), \\ \frac{dy}{dt} &= x(\rho - z) - y, \\ \frac{dz}{dt} &= xy - \beta z, \end{aligned} \quad (3)$$

with the parameters $\sigma = 10, \beta = 8/3, \rho = 28$ [Lor63]. The stretching and folding around the wings of the Lorenz attractor gives rise to the chaotic dynamics which yields an unpredictable time evolution (Fig. 1).

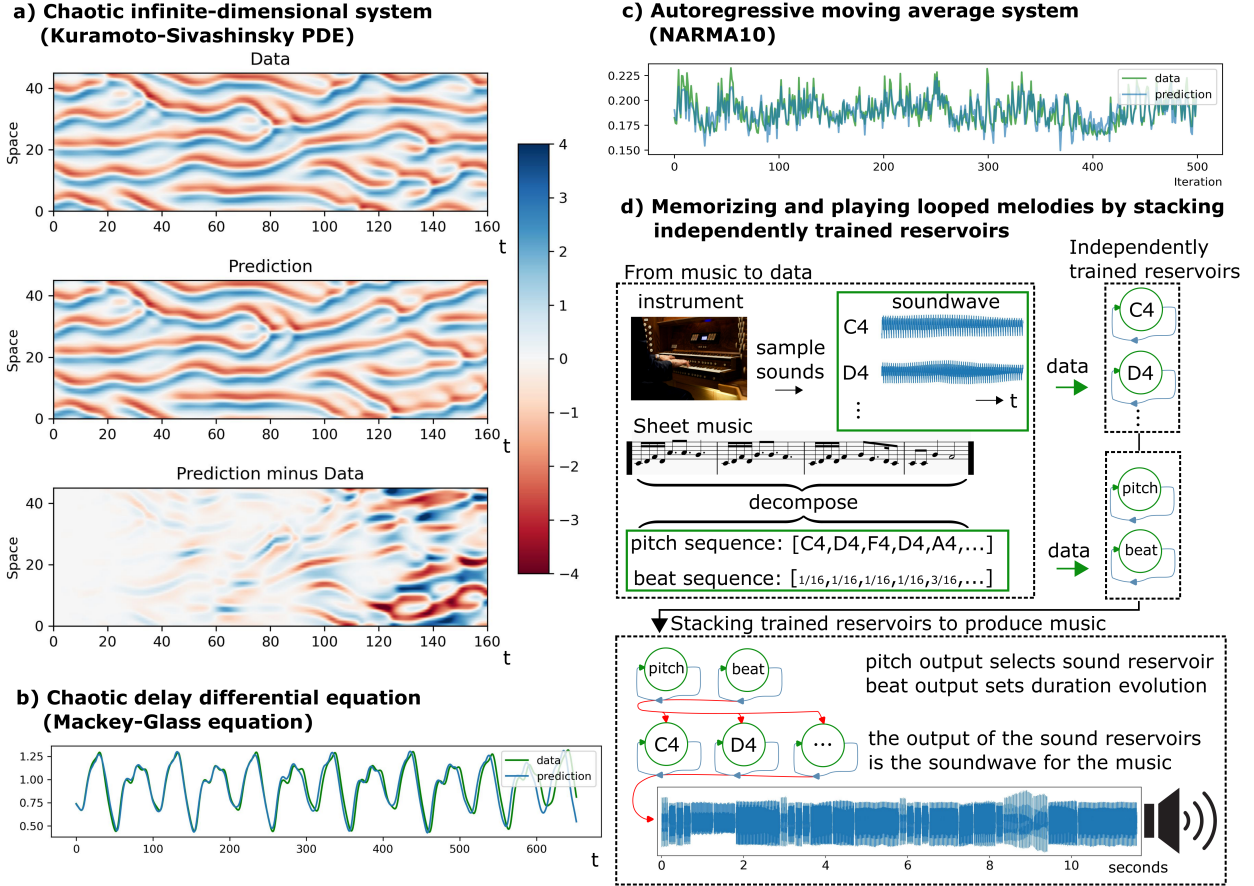


Figure 2: **Reservoir performance overview:** The learning tasks for (abd) concern the closed reservoir. Task (c) concerns a random input task and hence the reservoir is not studied in the closed setting. For task (d) videos have been included to show the inner workings of the reservoir.

For the reservoir, we take $N = 1000$ and consider the input-driven system (1) for $-25 \leq t < 0$ (Fig 1a), then train the system for $0 \leq t < 100$ (Fig. 1b), and finally switch to (2) for $t \geq 100$ (Fig. 1c). In the Supplementary Information a detailed description is given of the numerical scheme.

In (Fig. 2abc) we consider additional benchmark tests. The parameter configurations can be found in the Supplementary Information. Furthermore, in (Fig. 2d) we showcase memory capabilities of a multitude of closed reservoirs by designing an architecture where independently trained reservoirs are stacked such that as a collective they can play looped melodies, see the Supplementary Videos for the reservoirs evolution with audio. Finally, in the Supplementary Information we repeat all the experiments in this Article for another three-dimensional attractor given by the Rössler system for the generality of our arguments. However, here we will continue with the Lorenz system.

2.3 All-to-all coupling with linear complexity

Observe that computation of the full vector field in (1) has $O(N^2)$ -complexity. This is to be expected as the Kuramoto model describes an all-to-all coupling between oscillators. The so-called complex order parameter proposed by Kuramoto [Kur75] is given by $\frac{1}{N} \sum_{k=1}^N e^{i\theta_k}$. Writing the complex order as $r(t) \in \mathbb{R}$, $\Psi(t) \in \mathbb{S}$ satisfying

$$r(t)e^{i\Psi(t)} = \frac{1}{N} \sum_{k=1}^N e^{i\theta_k(t)}, \quad (4)$$

the coupling term in (1) can be rewritten as

$$\sum_{j=1}^N [\sin(\theta_j - \theta_k)] = r \sin(\Psi - \theta_k). \quad (5)$$

Substitution of (5) into (2) makes the computation of the vector field $O(N)$ -complexity. The numerical method to solve (2) preserves the linear complexity.

We note that in the simulations a slightly more efficient form of (4) is considered, see the Supplementary Information.

2.4 The bifurcation initiating learning

The reservoir is successful at the prediction task when the coupling parameter exceeds a critical value. The corresponding bifurcation can be understood via the complex order parameter (4). But before continuing we review the classical bifurcation that occurs in the Kuramoto model, (2) for $F = 0$, using the complex order parameter.

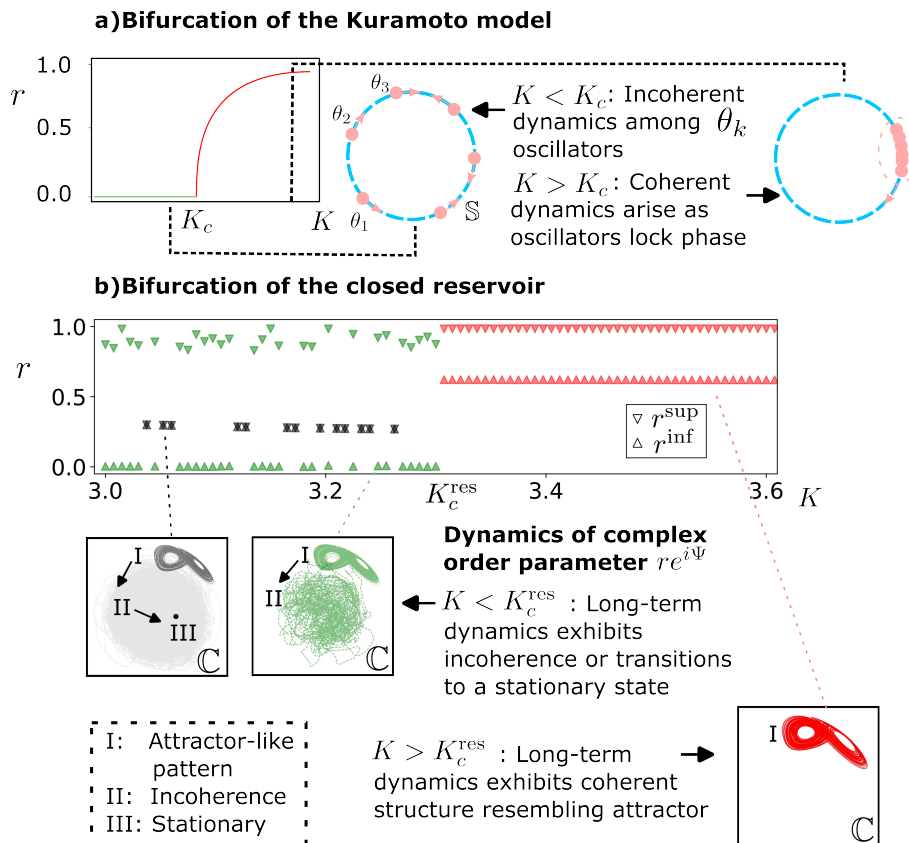


Figure 3: **The oscillators undergo a bifurcation when the coupling is sufficiently large for occurrence of synchronous dynamics.** In the reservoir the states expressed in the order parameter resemble the Lorenz attractor above a critical coupling.

The complex order parameter corresponds to the centroid of the phases and describes the collective rhythm produced by the oscillators [Str00]. The radius r determines the phase coherence of the oscillators and Ψ is the average phase. For r close to 0 the oscillators spread out over the circle and for r close to 1 the oscillators are clumped together (Fig. 3a).

For $t \rightarrow \infty$ Kuramoto observed that $r \rightarrow \rho_K$ for $N \rightarrow \infty$ such that for $K \leq K_c$ no coherence occurs as $\rho_K = 0$. But for $K > K_c$ we observe that $\rho_K > 0$ as the oscillators exhibit phase-locking (Fig. 3a). More specifically, for $K > K_c$ the order parameter rapidly increases to 1 as K is increased.

In the closed reservoir the bifurcation of r with respect to K differs from the bifurcation occurring in the Kuramoto model. In (Fig. 3b) we fix F for the reservoir. We observe that there exists a critical parameter K_c^{res} such that for $K > K_c^{\text{res}}$ the order parameter r exhibits oscillating behaviour which in $re^{i\Psi}$ appears Lorenz-like (Fig. 3b). For these parameters the prediction accurately approximates the target attractor for long-term evolution. For $K < K_c^{\text{res}}$ the imprinting of the dynamics on the reservoir becomes weaker and it transitions from Lorenz-like chaotic dynamics to a type of incoherence which corresponds to erratic motion in $re^{i\Psi}$. This incoherence can transition into the oscillators becoming stationary.

2.5 Collective intelligence

Individual oscillators θ_k can closely resemble the Lorenz time series under a linear transformation (Fig. 4a). Furthermore, selecting three oscillators we obtain an attractor that looks similar to the Lorenz attractor. However, these results are rather unsatisfying as we are cherry-picking from $N = 1000$ oscillators. For a more rigorous approach we require a method to study the oscillators as a whole. We will turn to r in (4) as a tool for understanding the collective dynamics.

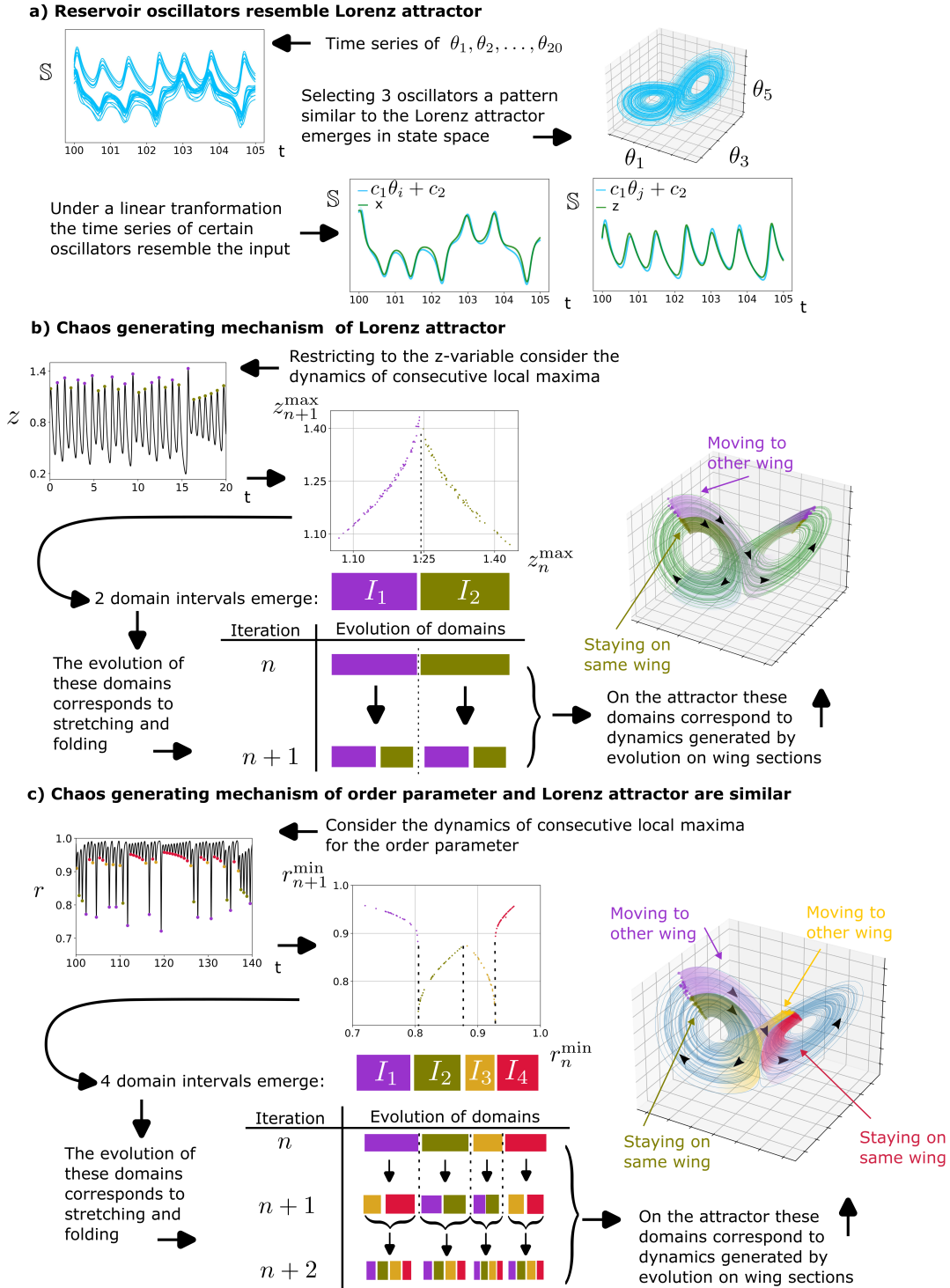


Figure 4: **Chaos generating mechanism of the target attractor is collectively learned by the oscillators:** The reservoir states resemble the input states. However, to properly evaluate all states we show that the chaos generating mechanism encoded in the order parameter is similar to the chaos generating mechanism in the Lorenz attractor.

Before continuing we present the classical procedure to expose chaos in the Lorenz system [Lor63]. Following the consecutive maxima of the z -variable, z_n^{\max} , we observe that the map corresponding to $z_n^{\max} \mapsto z_{n+1}^{\max}$ corresponds to stretching and folding (Fig. 4b). The stretching implies that solutions start close to each other but separate after sufficiently long time, referred to as sensitive dependence on initial conditions. The folding ensures that the motion does not diverge. Separating the domains of the map into I_1 and I_2 we can symbolically represent the sensitive dependence and then link the domains back to sections on the attractor.

We apply the previous procedure to the time series of r for the closed reservoir (Fig. 4c). Instead of following consecutive local maxima of r we consider consecutive minima, r_n^{\min} . Studying the dynamics of the map corresponding to $r_n^{\min} \mapsto r_{n+1}^{\min}$. We can identify four domains, I_1, I_2, I_3, I_4 . Applying the r map twice these domains are being stretched and folded until they cover the full domain (Fig. 4c). Additionally, the domains can be uniquely identified to staying on a wing or moving to the other wing (Fig. 4c). This indicates that the oscillators collectively learn as they identify as a whole the underlying dynamics. We note that this procedure also works for local maxima, see the Supplementary Information. However, minima are chosen for aesthetic purposes as the maxima are clumped together.

2.6 Forcing and coupling: the rise of synchronization and the collapse of internal geometry

By construction Equation (2) depends on the interaction between forcing and coupling. For the generalizability of the Kuramoto reservoir it is paramount that the performance does not sensitively depend on the parameters. We will consider the short-term prediction and long-term dynamics to determine the configuration flexibility.

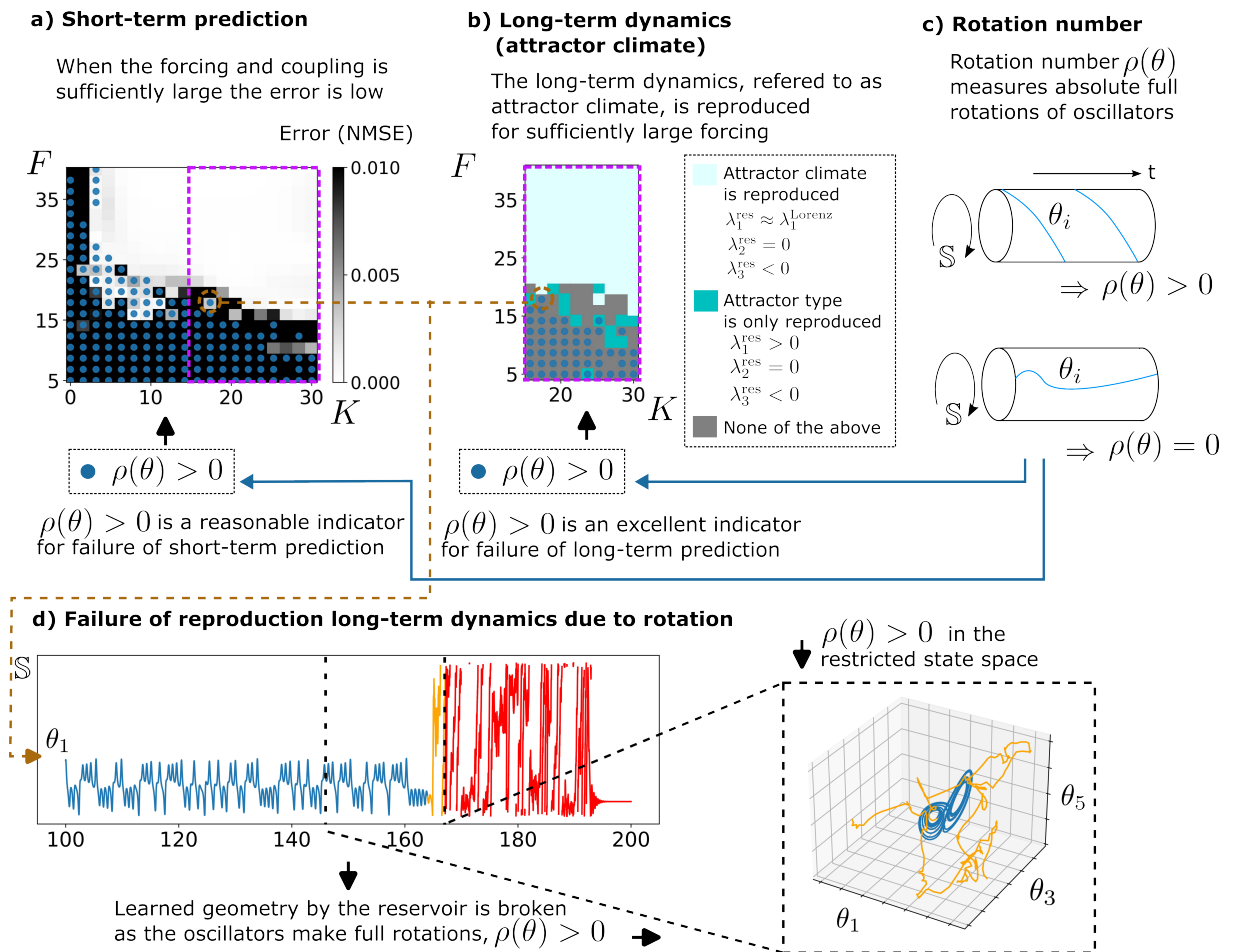


Figure 5: **The connection between forcing, coupling, synchronization and internal geometry:** Parameters leading to successful learning are abundant. Full rotations of the oscillators lead to destruction of the learned geometry from the target attractor.

For the short-term prediction we use the Normalized Mean Square Error (NMSE) averaged over the components for the time duration of a couple of oscillations around the wings (the time interval [100,102]), see Methods. In (Fig. 5a) we observe that above a certain threshold of F and K we obtain high performance. Note that for $K = 0$ the NMSE is large. This is to be expected since for $K = 0$ the oscillators are not coupled while the Lorenz equations (3) are coupled. Note that this shows that the learning capabilities of the collective are greater than the learning capabilities of the individual.

To study the long-term dynamics it is insufficient to consider an error measure on the prediction as the sensitive dependence on initial conditions of the Lorenz attractor ensures that solutions that start close to each other will separate. We use invariants that characterize chaos. Here, we compute Lyapunov exponents of (2) which is a common tool in the study of reservoirs [PLH⁺17]. Lyapunov exponents measure the rate of separation for trajectories that start close to each other. The time interval considered for computing Lyapunov exponent depends on their convergence. However, typically we consider about 10 times the duration that was used in the generation of the Lorenz attractor (time interval [100,1100]) (Fig. 1). Denote the reservoir's Lyapunov exponents by $\lambda_1^{\text{res}} \geq \lambda_2^{\text{res}} \geq \lambda_3^{\text{res}} \geq \dots$. The Lyapunov exponents for the Lorenz attractor are given by $\lambda_1^{\text{Lorenz}} \approx 0.91$, $\lambda_2^{\text{Lorenz}} = 0$, $\lambda_3^{\text{Lorenz}} \approx -14.57$. For the long-term dynamics we restrict to chaotic attractors of the reservoir which are of the same type as the Lorenz attractor, meaning that $\lambda_1^{\text{res}} > 0, \lambda_2^{\text{res}} = 0, \lambda_3^{\text{res}} < 0$. When $\lambda_1^{\text{res}} \approx \lambda_1^{\text{Lorenz}}$ we say that the attractor's climate has been reproduced [PLH⁺17]. We observe that the target attractor's climate is successfully reproduced when the forcing is sufficiently large (Fig. 5b). This fits our expectations since we would expect that synchronization improves with forcing. A more detailed Lyapunov exponent bifurcation diagram can be found in the Supplementary Information.

We note that the parameter c in (2), the input/feedback-loop strength, was not considered in this section. It requires fine-tuning but there is a parameter range in which the reservoir is successful. Additionally, from an application perspective we would expect that we can fully control the strength of the input/feedback-loop. When we consider sparse connectivity between the oscillators instead of all-to-all connectivity the successful region in (c, F, K) -parameter space greatly increases, see the Supplementary Information.

We conclude our results with investigating how the dynamics of (2) can lead to situations where the geometry of the input is not learned or forgotten as the reservoir is evolved. Observe that the solutions of (2) lie on the N -dimensional torus, \mathbb{T}^N , whereas the Lorenz attractor lies in \mathbb{R}^3 . We define the rotation number for an oscillator θ_k :

$$\rho(\theta_k) = \left\lfloor \frac{1}{2\pi} \left| \int_0^\infty \theta'_k(\tau) d\tau \right| \right\rfloor. \quad (6)$$

Examples are given in (Fig. 5c). We check for which parameters there exists an oscillator satisfying $\rho(\theta_k) > 0$. Returning to (Fig. 5b) we observe that $\rho(\theta_k)$ is a reasonable indicator for performance of short-term predictions with $\rho(\theta_k) > 0$ indicating high error and $\rho(\theta_k) = 0$ indicating low error. Then, returning to (Fig. 5c) we observe that climate reproducing reservoirs satisfying $\rho(\theta_k) > 0$ do not exist. Returning to (Fig. 5a) we observe that there are parameter values for which the indicator fails: $\rho(\theta_k) > 0$ but the short-term prediction accuracy is high. In (Fig. 5d) we evolve these oscillators for multitudes of the short-term prediction duration. Initially the oscillator resembles the input time-series but after a while the oscillator starts rotating. During this rotation the prediction leaves the attractor-pattern. As the reservoir is evolved the attractor-pattern is unraveled until it is forgotten and the reservoir becomes stationary.

3 Discussion

In this Article we presented a framework by which coupled oscillator networks can be harnessed as a linear time complexity, explainable, easy-to-configure, computational resource. We have shown that the classical model for phase-locking, the Kuramoto model, can be harnessed to solve learning tasks. Since the Kuramoto model is a foundational model for a wide variety of applications this Article provides the evidence that the full range of Kuramoto-like systems have learning capabilities. Hence, this work offers a direct path for scientific communities that makes use of Kuramoto-like systems to utilize them in the context of artificial intelligence.

Numerous works have shown the importance of synchronization in reservoir computers [LHO18, VAL21, LWSJ19, WYG⁺19]. This work puts forward a cornerstone by proposing that we can study synchroniza-

tion capabilities of weakly coupled, nearly identical limit-cycle oscillators within the context of reservoir computing. Moreover, in the setting of the Kuramoto reservoir we can use the technique from [OA08] to formulate the continuum limit for $N \rightarrow \infty$ and study the synchronization capabilities analytically, see the Supplementary Information.

There exist a variety of studies that have implemented Kuramoto-like systems for learning tasks. In [ZGF⁺23] pattern prediction tasks for a Kuramoto-like system is considered. The dependency on the input is introduced in the distance between oscillators. Reminiscent of Hopfield networks the connectivity of the network is altered until it can reproduce the input. In [CTS24] a Kuramoto reservoir presented with strong theoretical results, however it can only predict periodic inputs (sinus and triangle waves). In [SLP22] a singular Hopf oscillator is considered which is used to generate network nodes artificially using a delay-operation called multiplexing. Although a multiplexed Kuramoto reservoir could be investigated, it is preferable to increase the natural dimension of the reservoir as the information capabilities do not necessarily increase with respect to these artificial nodes. Oscillators networks can be trained to perform classification tasks. This is achieved by training the oscillators to synchronize to specific inputs. In [VLAA⁺17, VLGQ18] this task is performed using a low dimensional Kuramoto-like model where the natural frequencies are the weights and input of the network. The dynamics of Spin Torque Oscillators (STO) can be harnessed as a computational resource [TRAA⁺17, MLR⁺19, FFN⁺18, TTN⁺19, TKK⁺23]. In [GBMB21, FMW16] it is shown that the dynamics of coupled STOs can be modeled using a Kuramoto-like model.

A promising angle for the application of our framework is swarm dynamics. In [LASJ21] reservoir computing is performed with swarms but the dynamics of each individual depends only on spatial interactions. However, there are mobile oscillators whose movement is affected by their phases. For these systems the swarmalator model has been proposed [OHS17]. The governing equations come with a separate equation for the phases to which we can directly apply our reservoir framework. In [SGO24] it has been suggested that magnetic domain walls driven by pinning impurities can be modelled as swarmalators. These magnetic domain wall systems hold great promise as next generation memory.

References

- [AFG⁺08] T.M. Antonsen, R.T. Faghih, M. Girvan, E. Ott, and J. Plutig. External periodic driving of large systems of globally coupled phase oscillators. *Chaos: An Interdisciplinary Journal of Nonlinear Science*, 18(3), 2008.
- [AP00] A.F. Atiya and A.G. Parlos. New results on recurrent network training: unifying the algorithms and accelerating convergence. *IEEE transactions on neural networks*, 11(3):697–709, 2000.
- [BGGS80] G. Benettin, L. Galgani, A. Giorgilli, and J.M. Strelcyn. Lyapunov characteristic exponents for smooth dynamical systems and for hamiltonian systems; a method for computing all of them. part 1: Theory. *Meccanica*, 15:9–20, 1980.
- [Bol98] B. Bollobás. *Modern graph theory*. Springer, 1998.
- [CS08] L.M. Childs and S.H. Strogatz. Stability diagram for the forced kuramoto model. *Chaos: An Interdisciplinary Journal of Nonlinear Science*, 18(4):043128, 2008.
- [CTS24] H Chiba, K. Taniguchi, and T. Sumi. Reservoir computing with the kuramoto model. *arXiv:2407.16172*, 2024.
- [dJAT⁺23] T.G. de Jong, N. Akashi, T. Taniguchi, H. Notsu, and K. Nakajima. Virtual reservoir acceleration for cpu and gpu: Case study for coupled spin-torque oscillator reservoir. In *NeurIPS: ML with New Compute Paradigms Workshop*. NeurIPS, 2023.
- [DVB⁺21] A. Davies, P. Veličković, L. Buesing, S. Blackwell, D. Zheng, N. Tomašev, R. Tanburn, P. Battaglia, C. Blundell, A. Juhász, et al. Advancing mathematics by guiding human intuition with AI. *Nature*, 600(7887):70–74, 2021.
- [FFN⁺18] T. Furuta, K. Fujii, K. Nakajima, S. Tsunegi, H. Kubota, Y. Suzuki, and S. Miwa. Macro-magnetic simulation for reservoir computing utilizing spin dynamics in magnetic tunnel junctions. *Physical Review Applied*, 10(3):034063, 2018.

- [FMW16] V. Flovik, F. Macia, and E. Wahlström. Describing synchronization and topological excitations in arrays of magnetic spin torque oscillators through the kuramoto model. *Scientific reports*, 6(1):32528, 2016.
- [GBMB21] N. Garg, S.V.H. Bhotla, P.K. Muduli, and D. Bhowmik. Kuramoto-model-based data classification using the synchronization dynamics of uniform-mode spin hall nano-oscillators. *Neuromorphic Computing and Engineering*, 1(2):024005, 2021.
- [Hak83] H. Haken. At least one lyapunov exponent vanishes if the trajectory of an attractor does not contain a fixed point. *Physics Letters A*, 94(2):71–72, 1983.
- [HK70] A.E. Hoerl and R. W. Kennard. Ridge regression: Biased estimation for nonorthogonal problems. *Technometrics*, 12(1):55–67, 1970.
- [Jae01] H. Jaeger. The "echo state" approach to analysing and training recurrent neural networks—with an erratum note. *Bonn, Germany: German National Research Center for Information Technology GMD Technical Report*, 148(34):13, 2001.
- [Jae02] H. Jaeger. A tutorial on training recurrent neural networks, covering bppt, rtrl, ekf and the "echo state network" approach. Technical report, International University Bremen, 2002.
- [JEP⁺21] J. Jumper, R. Evans, A. Pritzel, T. Green, M. Figurnov, O. Ronneberger, K. Tunyasuvunakool, R. Bates, A. Židek, A. Potapenko, et al. Highly accurate protein structure prediction with alphafold. *Nature*, 596(7873):583–589, 2021.
- [JH04] H. Jaeger and H. Haas. Harnessing nonlinearity: Predicting chaotic systems and saving energy in wireless communication. *Science*, 304(5667):78–80, 2004.
- [KT76] Y. Kuramoto and T. Tsuzuki. Persistent propagation of concentration waves in dissipative media far from thermal equilibrium. *Progress of theoretical physics*, 55(2):356–369, 1976.
- [KT19] J.D.M.W.C. Kenton and L.K. Toutanova. Bert: Pre-training of deep bidirectional transformers for language understanding. In *Proceedings of NAACL-HLT*, pages 4171–4186, 2019.
- [Kur75] Y. Kuramoto. Self-entrainment of a population of coupled non-linear oscillators. In *International Symposium on Mathematical Problems in Theoretical Physics: January 23–29, 1975, Kyoto University, Kyoto/Japan*, pages 420–422. Springer, 1975.
- [Kur84] Y. Kuramoto. *Chemical turbulence*. Springer, 1984.
- [LASJ21] T. Lymburn, S.D. Algar, M. Small, and T. Jüngling. Reservoir computing with swarms. *Chaos: An Interdisciplinary Journal of Nonlinear Science*, 31(3), 2021.
- [LBAJ23] J.T. Lizier, F. Bauer, F.M. Atay, and J. Jost. Analytic relationship of relative synchronizability to network structure and motifs. *Proceedings of the National Academy of Sciences*, 120(37):e2303332120, 2023.
- [LBH15] Y. LeCun, Y. Bengio, and G. Hinton. Deep learning. *Nature*, 521(7553):436–444, 2015.
- [LHO18] Z. Lu, B.R. Hunt, and E. Ott. Attractor reconstruction by machine learning. *Chaos: An Interdisciplinary Journal of Nonlinear Science*, 28(6), 2018.
- [Lor63] E.N. Lorenz. Deterministic nonperiodic flow. *Journal of atmospheric sciences*, 20(2):130–141, 1963.
- [LPS15] S.K. Lam, A. Pitrou, and S. Seibert. Numba: A llvm-based python jit compiler. In *Proceedings of the Second Workshop on the LLVM Compiler Infrastructure in HPC*, pages 1–6, 2015.
- [LWSJ19] T. Lymburn, D.M. Walker, M. Small, and T. Jüngling. The reservoir’s perspective on generalized synchronization. *Chaos: An Interdisciplinary Journal of Nonlinear Science*, 29(9), 2019.
- [MG77] M.C. Mackey and L. Glass. Oscillation and chaos in physiological control systems. *Science*, 197(4300):287–289, 1977.

- [MLR⁺19] D. Marković, N. Leroux, M. Riou, F. Abreu Araujo, J. Torrejon, D. Querlioz, A. Fukushima, S. Yuasa, J. Trastoy, P. Bortolotti, et al. Dynamic effects on reservoir computing with a hopf oscillator. *Applied Physics Letters*, 114(1):012409, 2019.
- [Nak18] K. Nakajima. Reservoir computing: Theory, physical implementations, and applications. *IEICE Technical Report; IEICE Tech. Rep.*, 118(220):149–154, 2018.
- [Nak20] K. Nakajima. Physical reservoir computing: an introductory perspective. *Japanese Journal of Applied Physics*, 59(6):060501, 2020.
- [NFN⁺19] K. Nakajima, K. Fujii, M. Negoro, K. Mitarai, and M. Kitagawa. Boosting computational power through spatial multiplexing in quantum reservoir computing. *Physical Review Applied*, 11(3):034021, 2019.
- [OA08] E. Ott and T.M. Antonsen. Low dimensional behavior of large systems of globally coupled oscillators. *Chaos: An Interdisciplinary Journal of Nonlinear Science*, 18(3), 2008.
- [OHS17] K.P. O’Keeffe, H. Hong, and S.H. Strogatz. Oscillators that sync and swarm. *Nature communications*, 8(1):1504, 2017.
- [PC12] T.S. Parker and L. Chua. *Practical numerical algorithms for chaotic systems*. Springer Science & Business Media, 2012.
- [PJSF04] H.O. Peitgen, H. Jürgens, D. Saupe, and M.J. Feigenbaum. *Chaos and fractals: new frontiers of science*, volume 106. Springer, 2004.
- [PLH⁺17] J. Pathak, Z. Lu, B.R. Hunt, M. Girvan, and E. Ott. Using machine learning to replicate chaotic attractors and calculate lyapunov exponents from data. *Chaos: An Interdisciplinary Journal of Nonlinear Science*, 27(12), 2017.
- [Que24] D. Querlioz. Physics solves a training problem for artificial neural networks. *Nature*, 632(8024):264–265, 2024.
- [RDN⁺22] A. Ramesh, P. Dhariwal, A. Nichol, C. Chu, and M. Chen. Hierarchical text-conditional image generation with clip latents. *arXiv:2204.06125*, 2022.
- [Rös76] O.E. Rössler. An equation for continuous chaos. *Physics Letters A*, 57(5):397–398, 1976.
- [Sak88] H. Sakaguchi. Cooperative phenomena in coupled oscillator systems under external fields. *Progress of theoretical physics*, 79(1):39–46, 1988.
- [SGO24] G.K. Sar, D. Ghosh, and K. O’Keeffe. Solvable model of driven matter with pinning. *Physical Review E*, 109(4):044603, 2024.
- [SK86] H. Sakaguchi and Y. Kuramoto. A soluble active rotator model showing phase transitions via mutual entertainment. *Progress of Theoretical Physics*, 76(3):576–581, 1986.
- [SLP22] M.R.E.U. Shougat, X.F. Li, and E. Perkins. Dynamic effects on reservoir computing with a hopf oscillator. *Physical Review E*, 105(4):044212, 2022.
- [Str00] S.H. Strogatz. From kuramoto to crawford: exploring the onset of synchronization in populations of coupled oscillators. *Physica D: Nonlinear Phenomena*, 143(1-4):1–20, 2000.
- [SVM07] J.A. Sanders, F. Verhulst, and J. Murdock. *Averaging methods in nonlinear dynamical systems*, volume 59. Springer, 2007.
- [TKK⁺23] S. Tsunegi, T. Kubota, A. Kamimaki, J. Grollier, V. Cros, K. Yakushiji, A. Fukushima, S. Yuasa, H. Kubota, K. Nakajima, et al. Information processing capacity of spintronic oscillator. *Advanced Intelligent Systems*, 5(9):2300175, 2023.
- [TRAA⁺17] J. Torrejon, M. Riou, F. Abreu Araujo, S. Tsunegi, G. Khalsa, D. Querlioz, P. Bortolotti, V. Cros, K. Yakushiji, A. Fukushima, H. Kubota, S. Yuasa, M.D. Stiles, and J. Grollier. Neuromorphic computing with nanoscale spintronic oscillators. *Nature*, 547:428, 2017.
- [TTN⁺19] S. Tsunegi, T. Taniguchi, K. Nakajima, S. Miwa, K. Yakushiji, A. Fukushima, S. Yuasa, and H. Kubota. Physical reservoir computing based on spin torque oscillator with forced synchronization. *Applied Physics Letters*, 114(16), 2019.

- [TYH⁺19] G. Tanaka, T. Yamane, J.B. Héroux, R. Nakane, N. Kanazawa, S. Takeda, H. Numata, D. Nakano, and A. Hirose. Recent advances in physical reservoir computing: A review. *Neural Networks*, 115:100–123, 2019.
- [VAL21] P. Verzelli, C. Alippi, and L. Livi. Learn to synchronize, synchronize to learn. *Chaos: An Interdisciplinary Journal of Nonlinear Science*, 31(8), 2021.
- [VLAA⁺17] D. Vodenicarevic, N. Locatelli, F. Abreu Araujo, J. Grollier, and D. Querlioz. A nanotechnology-ready computing scheme based on a weakly coupled oscillator network. *Scientific reports*, 7(1):44772, 2017.
- [VLGQ18] D. Vodenicarevic, N. Locatelli, J. Grollier, and D. Querlioz. Nano-oscillator-based classification with a machine learning-compatible architecture. *Journal of Applied Physics*, 124(15), 2018.
- [Win67] A.T. Winfree. Biological rhythms and the behavior of populations of coupled oscillators. *Journal of theoretical biology*, 16(1):15–42, 1967.
- [Win01] A.T. Winfree. *The geometry of biological time*, volume 2. Springer, 2001.
- [WS98] D.J. Watts and S.H. Strogatz. Collective dynamics of "small-world" networks. *Nature*, 393(6684):440–442, 1998.
- [WYG⁺19] T. Weng, H. Yang, C. Gu, J. Zhang, and M. Small. Synchronization of chaotic systems and their machine-learning models. *Physical Review E*, 99(4):042203, 2019.
- [ZGF⁺23] Z. Zuo, Z. Gan, Y. Fan, V. Bobrovs, X. Pang, and O. Ozolins. Self-evolutionary reservoir computer based on kuramoto model. *arXiv:2301.10654*, 2023.

Supplementary Information

S1 Introduction

In S2-S6 we provide extensive supporting results (benchmarks, theoretical analyses, numerical schemes, explorations of future topics, etc.) to each result section in the main paper with the exception of the music reservoir in (Fig. 2d) of the main paper. We have devoted a separate section to this reservoir, Section S7. In Section S8, we reproduce all the experiments in the main paper for a system similar to the Lorenz system, the Rössler system.

Note on the repository: This work is accompanied by a repository which contains the code to run the experiments and generate the data as well as a database for parameter-configurations. The repository is organized by the sections in the main paper and this document.

S2 Supplementary Information to Subsection 2.2

S2.1 Reservoir framework

We introduce the details of the framework and notation that will be used throughout these materials. In Table S1 we present a summary of parameters.

We consider an input function $u : \mathbb{R} \rightarrow \mathbb{R}^M$. The governing equations take the form

$$\frac{d\theta_k}{dt} = \omega_k + \sum_{j=1}^N \Gamma_{jk}(\theta_j - \theta_k) + F \sin(cu_{v_k} - \theta_k), \quad 1 \leq k \leq N \quad (7)$$

with $\theta_k \in \mathbb{S} := \mathbb{R}/2\pi\mathbb{Z}$ and $\Gamma_{jk} : \mathbb{S} \rightarrow \mathbb{R}$ the interaction function. In the setting of the Kuramoto reservoir we have that $\Gamma_{jk}(\theta_j - \theta_k) = \frac{K}{N} \sin(\theta_j - \theta_k)$. We follow the classical steps to constructing and evaluating a reservoir.

1. **Wipe-out:** We consider the initial value problem corresponding to Equation (1) and compute the solution for all $t \in [-T_{\text{wipe}}, 0)$.
2. **Training:** We continue the solution for all $t \in [0, T_{\text{train}})$. We consider a yet-to-be-defined $f : \mathbb{T}^N \rightarrow \mathbb{R}^{N_{\text{ro}}}$, referred to as read-out function. We find a $W^{\text{out}} \in \mathbb{R}^{M \times N_{\text{ro}}}$ such that $W^{\text{out}} f(\theta(t))$ predicts the input at the corresponding time. The numerical scheme will be discussed in S2.2. Let us make the computation of W^{out} explicit. Assume T_{train} to be a multiple of h_{res} and define $n_{\text{train}} := T_{\text{train}}/h_{\text{res}}$. We define $\Theta = (\theta(0), \theta(h_{\text{res}}), \dots, \theta(h_{\text{res}}(n_{\text{train}} - 1))) \in \mathbb{S}^{N \times n_{\text{train}}}$ and $U = (u(0), u(h_u), \dots, u(h_u(n_{\text{train}} - 1))) \in \mathbb{R}^{M \times n_{\text{train}}}$. Then we find

$$W' = \arg \min_W \|W \hat{f}(\Theta) - U\|_2^2 + \varepsilon \|W\|_2^2, \quad (8)$$

with $\varepsilon > 0$ the ridge-regression constant and $\hat{f} : \mathbb{T}^N \times n_{\text{train}} \rightarrow \mathbb{R}^{N_{\text{ro}} \times n_{\text{train}}}$ given by applying f on the components in the time-direction. We compute W' in (8) using ridge regression [HK70]:

$$W' = U \hat{f}(\Theta)^\top (\hat{f}(\Theta) \hat{f}(\Theta)^\top + \varepsilon I)^{-1},$$

with I being an $N_{\text{ro}} \times N_{\text{ro}}$ identity matrix.

3. **Testing:** In the governing ODE we substitute the input u by $W^{\text{out}} f(\theta)$. Let us denote the new dependent variable by $\hat{\theta}$. Then we compute the solution with initial value $\hat{\theta}(T_{\text{train}}) = \theta(T_{\text{train}})$ for all $t \in [T_{\text{train}}, T_{\text{train}} + T_{\text{test}})$ which is used to evaluate the performance of the reservoir. More specifically, we compute $\hat{\theta}(t + (i - 1)h_{\text{res}})$, evaluate $\hat{u}(t + (i - 1)h_u) := W^{\text{out}} f(\hat{\theta}(t + (i - 1)h_{\text{res}}))$ for $i = 1, 2, \dots, n_{\text{test}}$ with $n_{\text{test}} = T_{\text{test}}/h_{\text{res}}$ and then compute the error between \hat{u}, u using the Normalized Mean Square Error (NMSE):

$$\text{NMSE} := \frac{1}{M} \sum_{j=1}^M \frac{\sum_{i=1}^{n_{\text{test}}} |u_j(t_i) - \hat{u}_j(t_i)|^2}{\sum_{i=1}^{n_{\text{test}}} |u_j(t_i)|^2}, \quad t_i := T_{\text{test}} + (i - 1)h_u.$$

Observe that the numerical scheme used to solve the $\hat{\theta}$ -equation needs to take into account the discrete nature of the prediction map of u given by $W^{\text{out}} f(\hat{\theta})$. The scheme will be discussed in Section S2.2.

Symbol	Definition
\mathbb{S}	$\mathbb{R}/2\pi\mathbb{Z}$
\mathbb{T}^N	$\underbrace{\mathbb{S} \times \cdots \times \mathbb{S}}_{N\text{-times}}$
F	forcing constant
K	coupling constant
c	input strength constant
Γ_{jk}	interaction function for θ_j and θ_k
f	read-out function $f : \mathbb{T}^N \rightarrow \mathbb{R}^{N_{ro}}$
N	number of oscillators
M	input dimension
ε	ridge regression constant
h_{res}	reservoir time-step
h_u	input time-step
T_{wipe}	duration wipe-out phase given by multiple of h_{res} (time-interval given by $[-T_{wipe}, 0)$)
n_{wipe}	$\lfloor T_{wipe}/h_{res} \rfloor \in \mathbb{N}$
T_{train}	duration training phase given by multiple of h_{res} (time-interval given by $[0, T_{train})$)
n_{train}	$\lfloor T_{train}/h_{res} \rfloor \in \mathbb{N}$
T_{test}	duration test phase given by multiple of h_{res} (time interval given by $[T_{train}, T_{train} + T_{test})$)
n_{test}	$\lfloor T_{test}/h_{res} \rfloor \in \mathbb{N}$

Table S1: Summary of parameters.

S2.2 Numerical scheme reservoir

The time-step h_{res} is exclusively used by the states θ and the time-step h_u is exclusively used by the input. Hence, for notational convenience we drop the subscripts of h .

We consider an input time series sampled with $\frac{1}{2h}$ -frequency. Let $u^{(j)} = u(t_0 + jh)$ with $j = 0, 1/2, 1, 3/2, 2, \dots$. We first consider the reservoir during the wipe-out and training-stage. We will write the governing equations as $\frac{d\theta}{dt} = F(\theta, u)$ with F denoting the vector field. The numerical approximation of $\theta(t_0 + ih)$ is denoted by $\theta^{(i)}$ with $i = 0, 1, 2, \dots$. Then, we consider the Runge-Kutta 4th order (RK4) for the wipe-out and training phase:

$$\begin{aligned}
k_1 &= hF(\theta^{(i)}, u^{(i)}), \\
k_2 &= hF(\theta^{(i)} + k_1/2, u^{(i+1/2)}), \\
k_3 &= hF(\theta^{(i)} + k_2/2, u^{(i+1/2)}), \\
k_4 &= hF(\theta^{(i)} + k_3, u^{(i+1)}), \\
\theta^{(i+1)} &= \theta^{(i)} + (k_1 + 2k_2 + 2k_3 + k_4)/6.
\end{aligned} \tag{9}$$

During training we compute a g such that $g(\theta^{(i)}) \approx u^{(i)}$. We define $G(\theta^{(i)}) = F(\theta^{(i)}, g(\theta^{(i)}))$ and consider the following scheme for testing:

$$\begin{aligned}
k_1 &= hG(\theta^{(i)}), \\
k_2 &= hG(\theta^{(i)} + k_1/2), \\
k_3 &= hG(\theta^{(i)} + k_2/2), \\
k_4 &= hG(\theta^{(i)} + k_3), \\
\theta^{(i+1)} &= \theta^{(i)} + (k_1 + 2k_2 + 2k_3 + k_4)/6.
\end{aligned}$$

Another possible scheme for the testing phase is

$$\begin{aligned}
k_1 &= hF(\theta^{(i)}, g(\theta^{(i)})) \\
k_2 &= hF(\theta^{(i)} + k_1/2, g(\theta^{(i)})) \\
k_3 &= hF(\theta^{(i)} + k_2/2, g(\theta^{(i)})) \\
k_4 &= hF(\theta^{(i)} + k_3, g(\theta^{(i)})) \\
\theta^{(i+1)} &= \theta^{(i)} + (k_1 + 2k_2 + 2k_3 + k_4)/6
\end{aligned} \tag{10}$$

This scheme can be interpreted as RK4 in θ and RK1 in u .

Observe that whenever $M \ll N$ these test phase schemes will run in $O(N)$.

S2.3 Reservoir configuration for Lorenz system

In Table S2 we present the parameters used in the main experiment.

Symbol	Value
N	1000
M	3
F	37.545
K	20.680
c	1.159
ε	10^{-5}
h_{res}	10^{-2}
h_{u}	10^{-2}
T_{wipe}	25
T_{train}	100

Table S2: Summary of parameters for Lorenz prediction task. We note that K, F are typically used as bifurcation parameters. Hence, the reported K, F are only used in (Fig. 1) of the main paper. We note that the input has been scaled by 30.92

The parameters were found using random search by sampling uniformly over parameter intervals. The c parameter appears to be important. Considering a value in $[0.9, 1.25]$ yields good results. We rescaled the input variable by dividing the input by 30.92. These values scale the input to a range in $[-\pi/2, \pi/2]$. The ω_k are sampled from a normal distribution $2\pi\mathcal{N}(\mu, \sigma)$. The μ and σ did not have a major impact on the performance so we just fixed them to 1. We fixed $N = 1000$ as it is commonly used in the literature but we obtain similar performance for $N = 500$. Additionally, $N = 1000$ is commonly chosen in the Kuramoto literature for when the system exhibits continuum limit behaviour [AFG⁺08].

Let ω and v denote the N -dimensional vectors corresponding to ω_k and v_k , respectively. We did not observe qualitatively different results for other ω and v .

S2.3.1 Data sets

The Lorenz system was computed with RK4 using time-step $\Delta t = 1/2000$. We removed transients. We note that in all Lorenz system related figures in the main paper and this document the input has been divided by 30.92 which is the divisor of c divided by 10^3 .

S2.4 Read-out functions

We investigated the performance of the following read-out functions:

1. $f(\theta) = [1, \sin(\theta)] \in \mathbb{R}^{N+1}$,
2. $f(\theta) = [1, \sin(\theta), \cos(\theta)] \in \mathbb{R}^{2N+1}$,
3. $f(\theta) = [1, \sin(\theta), \sin^2(\theta)] \in \mathbb{R}^{2N+1}$.

Performance was measured by sampling uniformly over all parameters, excluding N, h, μ, σ which were taken as in Section S2.3, and then measuring NMSE of the prediction during testing.

In Table S3 we arrange the performance from low to high. The read-out function 3. has most consistently high performance. We note that this read-out function is inspired by [PLH⁺17, LHO18] in which linear and quadratic terms are considered.

Read-out	NMSE < 0.01
[1, sin(θ)]	0.05%
[1, sin(θ), cos(θ)]	30.10%
[1, sin(θ), sin ² (θ)]	52.45%

Table S3: Performance of different read-out functions for $4 \cdot 10^3$ random samples over the parameter space.

S2.5 Comment on sampling natural frequencies from Cauchy distribution

Classically the Kuramoto model is considered with ω_k sampled from a Cauchy distribution:

$$g(\omega) = \frac{\Delta_0}{\pi((\omega - \omega_0)^2 + \Delta_0^2)}, \quad (11)$$

with ω_0, Δ_0 parameters. This is because the singularity of the distribution allows us to find an explicit expression in terms of an ODE for the order parameter when considering $N \rightarrow \infty$ [OA08].

Cauchy distributions have flat tails compared to normal distributions. This appears to affect the performance of the reservoir. More specifically, if we would consider $N = 1000$, $\omega_0 = \Delta_0 = 1$ then we are bound to find a couple of frequencies in $O(10)$. These large frequencies appear to negatively affect the performance. By considering Δ_0 much smaller such as $\Delta_0 = 0.01$ this problem can be circumvented.

S2.6 Additional benchmark tests

We consider additional benchmarks for the Kuramoto reservoir. We used a primitive random search algorithm to discover suitable parameters. Hence, these parameters could still be improved on. The exact configurations can be found in the repository.

We consider input time-series generated by three different processes: Partial Differential Equation (PDE), time delay ordinary differential equation and Autoregressive Moving Average model (ARMA).

a) Kuramoto-Sivashinsky (KS) equations: We consider a PDE given by the fourth-order KS-equations [KT76]:

$$\frac{\partial y}{\partial t} + \frac{1}{2} \frac{\partial y^2}{\partial x} + \frac{\partial^2 y}{\partial y^2} + \frac{\partial^4 y}{\partial x^4} = 0,$$

on the periodic domain given by $y(t, 0) = y(t, L)$ with $L = 45$. The input for the reservoir is given by $u_i(t) = y(t, i\Delta x)$ with $\Delta x = L/M$, $i = 1, 2, \dots, M$. General reservoir parameters are reported in Table S4. We note that here the performance depends strongly on v_k .

Parameter	Value
N	9000
M	50
F	47.27
K	32.17
c	0.271
h_{res}	0.01
h_u	0.2
$f(\theta)$	[1, sin(θ), sin ² (θ)]
ε	10^{-5}
n_{wipe}	5000
n_{train}	$20 \cdot 10^3$
n_{test}	800

Table S4: Summary of parameters for Kuramoto-Sivashinsky: NMSE = 0.56

b) Mackey-Glass (MG) equations [MG77]: The MG delay differential equation are given by :

$$\frac{dy(t)}{dt} = \frac{ay(t-\tau)}{1+y^n(t-\tau)} + by(t),$$

with the parameters $\tau = 17$ and $(a, b, n) = (0.2, 0.1, 10)$. The input for the reservoir is 1-dimensional and is given by $u(t) = y(t)$. General reservoir parameters are reported in Table S4. We note that to get the finer structure of the MG-equations we sampled ω_k from the normal distribution with $\mu = 1, \sigma = 9$.

Parameter	Value
N	1000
F	68.5
K	52.2
c	0.872
h_{res}	0.002
h_u	0.816
$f(\theta)$	$[1, \sin(\theta), \sin^2(\theta)]$
ε	10^{-7}
n_{wipe}	2200
n_{train}	10^3
n_{test}	800

Table S5: Summary of parameters for Mackey-Glass: NMSE = $9 \cdot 10^{-3}$

c) NARMA10 [AP00]: Finally, we consider a nonlinear ARMA model. Given a uniformly random input $u^k \in [-1, 1]$ the NARMA10 model is defined as

$$y^{k+1} = \alpha y^k + \beta y^k \sum_{i=0}^9 y^{k-i} + \gamma v^{k-9} v^k + \delta,$$

$$v^k = 0.2 \frac{u^k + 1}{2},$$

where subscript k indicates the k th time-step, $(\alpha, \beta, \gamma, \delta) = (0.3, 0.05, 1.5, 0.1)$, and the input u^k is biased and scaled to $v^k \in [0.0, 0.2]$ to avoid divergence. Given u^k and y^k for $n_{\text{wipe}} \leq k < n_{\text{train}}$ the task is to predict y^k given u_k for $n_{\text{train}} \leq k < n_{\text{test}}$. General reservoir parameters are reported in Table S6. An RK1-scheme is used because of the discontinuity of the input. We note that the test length used for the test error calculation is much longer than the test prediction given in the benchmark figure of the main paper.

Parameter	Value
N	500
F	14.3
K	1
c	0.1
h_{res}	0.1
$f(\theta)$	$[1, \sin(\theta)]$
ε	10^{-11}
n_{train}	$2 \cdot 10^3$
n_{test}	$2 \cdot 10^3$

Table S6: Summary of parameters for NARMA10: NMSE = $1.4 \cdot 10^{-3}$

S2.6.1 Comparing performance to Echo State Network (ESN) for NARMA10

Let us consider the conventional (discrete) ESN [JH04, Jae02, Jae01]. Let x_i^k be the activation of the i th reservoir node at time-step k . Denote the reservoir weights connecting the i th node to the j th node by w_{ij} . The weights are uniformly randomly sampled from $[-1, 1]$. However, a spectral radius ρ is imposed

on the resulting weight matrix. There are input weights connected to the i th input by w_i^{in} which are uniformly sampled from $[-\sigma, \sigma]$. The trainable weights will be denoted by w_i^{out} which will be obtained using ridge regression. The discrete time evolution is given by

$$\begin{aligned} x_i^k &= f \left(\sum_{j=1}^N w_{ij} x_j^{k-1} + w_i^{\text{in}} u^k \right), \\ \hat{y}^k &= \sum_{i=0} w_i^{\text{out}} x_i^k, \end{aligned}$$

where we take $x_0^k = 1$ so that the corresponding weight becomes a bias term and we consider $f : \mathbb{R} \rightarrow \mathbb{R}$ given by $f(x) = \tanh(x)$.

Observe that evolving ESN has $O(N^2)$ -complexity and recall that computation of the vector field for the Kuramoto reservoir has $O(N)$ -complexity. Hence, if we want to compare the Kuramoto reservoir with configuration given by Table S6 we need to consider an RK1-scheme for the Kuramoto reservoir and ESN with $N = 23$. For the NARMA task we perform a grid search for ESN using the methodology described in Appendix B of [NFN⁺19]. We find that ESN achieves NMSE = $7.9 \cdot 10^{-4}$ which is significantly smaller than the Kuramoto reservoir which achieves NMSE $1.4 \cdot 10^{-3}$. However, for ESN with $N = 10$ we obtain NMSE = $1.6 \cdot 10^{-3}$ and for Kuramoto reservoir with $N = 100$, configuration as in Table S6 and with 2-decimal optimized c , which is $c = 0.15$, also gives NMSE = $1.6 \cdot 10^{-3}$.

Let us note that this is not a fair comparison because NARMA10 is a discrete task. Hence, a continuous reservoir such as the Kuramoto reservoir is expected to perform worse than a discrete reservoir such as conventional ESN. Additionally, the coupling strength in the Kuramoto reservoir is taken constant whereas ESN has random internal weights. Hence, from a connectivity perspective ESN is richer than the network of the Kuramoto reservoir. Of course richer network connectivity classes can be considered for the Kuramoto model, see Section S2.7.

S2.6.2 Comments on initial condition

Typically the initial condition is chosen as $\theta_i(-T_{\text{wipe}}) = 2\pi(i-1)/(N-1)$. For N large this means in terms of the complex order parameter, $z = r e^{i\Psi}$, that $0 < |z(-T_{\text{wipe}})| \ll 1$. The complex order parameter for initial conditions sampled uniformly from $[0, 2\pi)$ will have similar properties and similar performance. Additionally, it appears when the embedded attractor in the reservoir states space is represented in the complex order parameter it is located in the right half-plane. Observe that $z(-T_{\text{wipe}})$ is also located in the right half-plane.

We observe that there is a significant dip in performance for MG and NARMA10 when we consider randomly sampled initial conditions. However, this can be resolved by considering a longer wipe-out phase, $n_{\text{wipe}} = 5000$ which is significantly larger than what is used for ESN in the literature. Averaging over 10 uniformly sampled random initial conditions we obtain for MG that NMSE = $\mu \pm \sigma = 1.1 \cdot 10^{-2} \pm 7 \cdot 10^{-3}$ and for NARMA10 that NMSE = $\mu \pm \sigma = 2.0 \cdot 10^{-3} \pm 8 \cdot 10^{-4}$. For KS we already considered $n_{\text{wipe}} = 5000$ and the NMSE barely varies for random initial conditions.

S2.6.3 General comments on improving performance

The Kuramoto reservoir as introduced in the main paper is the *vanilla* reservoir. There are a number of aspects that can be configured to improve performance: distribution for natural frequencies (for example, in the case of MG a bimodal distribution appears to improve performance, also see Section S2.5), interaction function, oscillator connectivity. The last two points will be discussed in the next section.

S2.7 Kuramoto reservoir variations

In this section we consider Kuramoto-like systems to which we apply the reservoir framework as presented in S2.1. More specifically, we consider Equation (1) for different Γ_{jk} . The first is the Kuramoto-Sakaguchi model [SK86]:

$$\Gamma_{jk}(\theta_j - \theta_k) = \frac{K}{N} \sin(\theta_j - \theta_k + \alpha). \quad (12)$$

We consider the case $\alpha = 0.1$ and obtain similar performance result compared to the Kuramoto reservoir we do not report on the details and refer to the accompanied code. Kuramoto-Sakaguchi model is a more general form of the Kuramoto model. Hence, this supports generalizability of the framework.

The Kuramoto model describes all-to-all coupling. Instead we can consider connectivity described by an arbitrary graph:

$$\Gamma_{jk}(\theta_j - \theta_k) = a_{jk} \sin(\theta_j - \theta_k) \quad (13)$$

with $A = (a_{jk}) \in \mathbb{R}^{N \times N}$ the adjacency matrix of the graph describing the connectivity between θ . Let us explore the performance based on the connectivity of A . We sample A from a graph model, the parameters c, F, K from a uniform distribution, $\omega \in 2\pi\mathcal{N}$ and then investigate the corresponding performance distributions in NMSE. All remaining parameters are fixed and given by the values in Table S2. For the data set we consider the Lorenz time-series with $n_{\text{test}} = 200$. We will sample A from the following graph models:

- N -node Erdős-Renyi random graph model [Bol98] with each edge included in the graph with probability $p = 0.1$;
- N -node regular graph model with degree 100;
- N -node Watts-Strogatz model [WS98], random graph model with small-world properties, with mean degree $m = 100$ and edge-rewiring probability $p = 0.5$.

We note that the regular graph model is not a random graph model. Note that the vertex degree distribution of the random graph model has mean 99.9. which is close to the mean degree of the regular graph model and Watts-Strogatz model. The performance results are displayed in Table S7. The random graph models have the best performance. Notably the regular graph model already outperforms the vanilla Kuramoto reservoir given by the all-to-all connected graph. We also performed experiments for connected graphs sampled from Watts-Strogatz. The performance for these connected graphs yields similar performance to Erdős-Renyi over the ranges considered in Table S7.

	all-to-all	Erdős-Renyi	regular	Watts-Strogatz
NMSE < 10^{-2}	43%	73%	68%	73%
NMSE < 10^{-3}	22%	63%	52%	58%
NMSE < 10^{-4}	4%	27%	20%	27%

Table S7: Performance of short-time prediction for different graph models: results precise up to $\pm 1\%$

S3 Supplementary Information to Subsection 2.3

S3.1 Hardware and computational speed

The CPU used for the experiments is an AMD Ryzen 9 5950X (16-core). The code was written in Python and the module Numba was used as an acceleration tool. Wipe-out, training and testing for a test length of $2 \cdot 10^5$ with the parameters in Table S2 can be performed in approximately 15 seconds. The procedures in [dJAT⁺23] are used to accelerate the computations.

S3.2 $O(N)$ vector field used in experiments

In none of the experiments we need to explicitly compute Ψ . So it makes more sense to write

$$\sum_{j=1}^N \sin(\theta_j - \theta_k) = R_1(\theta) \cos(\theta_k) - R_2(\theta) \sin(\theta_k), \quad (14)$$

where $R_1(\theta) = \sum_{j=1}^N \sin(\theta_j)$, $R_2(\theta) = \sum_{j=1}^N \cos(\theta_j)$. Substitution into (1) makes the computation of the vector field $O(N)$ -complexity.

S4 Supplementary Information to Subsection 2.4

S4.1 Bifurcation in K for fixed F : increasing ε

When we increase the ridge regression constant from $\varepsilon = 10^{-5}$, used in the main paper (Table S2), to $\varepsilon = 10^{-3}$ new dynamics appear in the learning bifurcation diagram (Fig. S1). Recall that we defined the critical parameter as the smallest K for which the order parameter exhibits long-term Lorenz-like dynamics. We observe that the critical parameter for $\varepsilon = 10^{-5}$ is around 3.3 which is smaller than than the critical parameter for $\varepsilon = 10^{-3}$ which is around 4.8 (Fig. S1a).

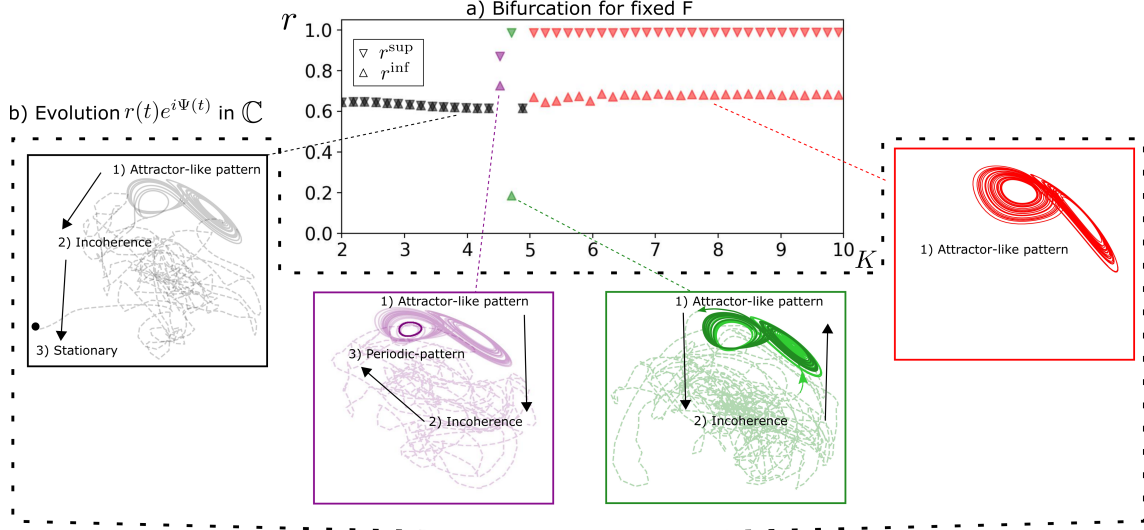


Figure S1: Bifurcation in K for $F = 35$ with $\varepsilon = 10^{-3}$

Comparing (Fig. S1a) to the bifurcation in the main paper we observe that a transition to a permanent incoherent state does not occur. However, in (Fig. S1b) we do observe that the motion can alternate between attractor-like pattern and incoherence. Notably decreasing K we obtain a configuration where the complex order parameter converges to periodic motion inside the lobes of the Lorenz-like wings, the purple box (Fig. S1)

S4.2 Bifurcation in F for fixed K

Returning to the parameters considered in the main paper (Table S2) we now consider the bifurcation in F for fixed K .

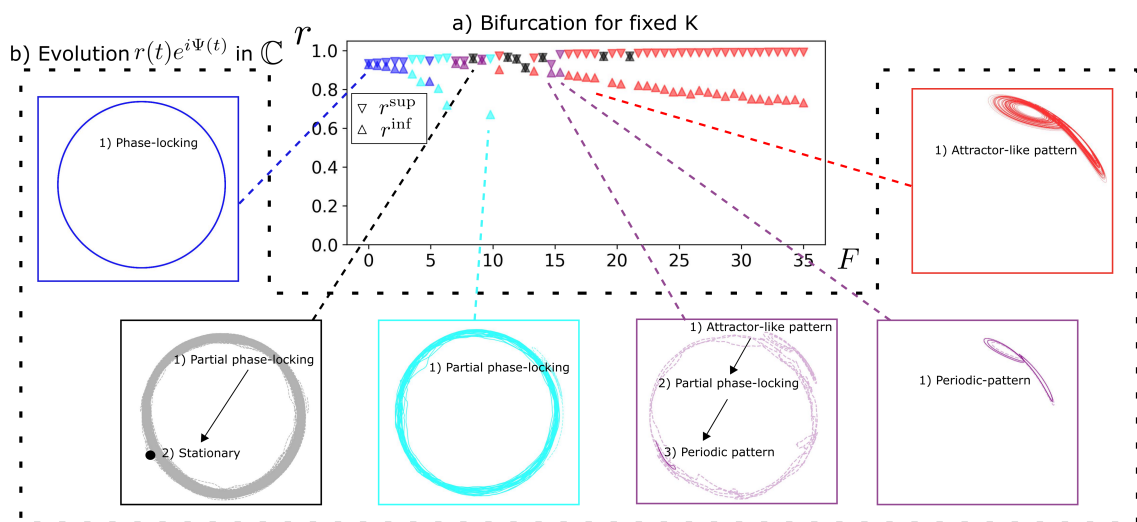


Figure S2: Bifurcation in F for $K = 20$ with $\varepsilon = 10^{-5}$

In short the bifurcation occurs as the result of the phase-locking state losing its stability for sufficiently large F . Although periodic motion of the complex order parameter can occur for a range of F (Fig. S2) when F is sufficiently large the complex order parameter converges to a Lorenz-like attractor.

S4.3 Numerical issues related to sensitive dependence on initial conditions

The bifurcations in this section require the study of the long-term dynamics of solutions. To accelerate the computational speed throughout the paper the Numba module is used [LPS15]. When the code is compiled, Numba can change the order of computations to optimize the computational speed. Hence, depending on the Numba version the quantitative properties of the solutions can be affected. This specifically concerns the transition times of the solutions in the bifurcation diagrams of this section.

S4.4 Continuum limit Kuramoto reservoir

S4.4.1 Classical forced Kuramoto equations

The governing equation draw inspiration from the classical forced Kuramoto equations:

$$\frac{d\theta_k}{dt} = \omega_k + \frac{K}{N} \sum_{j=1}^N \sin(\theta_j - \theta_k) + F \sin(ct - \theta_k). \quad (15)$$

In the context of the main article we have that $u : \mathbb{R} \rightarrow \mathbb{T}$ given by $u(t) = ct$.

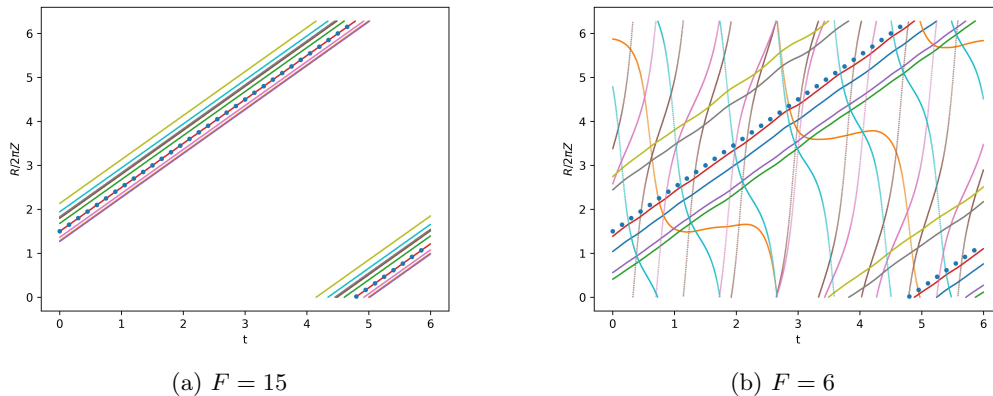


Figure S3: Let $u : \mathbb{R} \rightarrow \mathbb{T}$ be given by $u(t) = ct$ with $c = 1$, the blue dotted line in the figures, and $K = 1$. Then, for F sufficiently large (a) the states θ are entrained with u . For F sufficiently small (b) solutions can break away from u .

For sufficiently large F the oscillators θ_k lock to u (Fig. S3a). As F is decreased oscillators start breaking free from u (Fig. S3b).

S4.4.2 Forced Kuramoto equations as reservoir

The prediction task is given by the input $u(t) = ct$. We will formulate a procedure that does not require a training phase. More specifically, we present an explicit function for the prediction that is independent of c .

Relying on the techniques developed in [CS08, OA08, AFG⁺08] we can consider the continuum limit equations (15), $N \rightarrow \infty$, for the complex order parameter, $z := \frac{1}{N} \sum_{k=1}^N e^{i\theta_k}$, by the considering so-called Ott-Antonsen ansatz. We need to assume that ω_k are sampled from a Cauchy distribution (11). We set $\Delta_0 = 1$ as it turns out we can scale away Δ_0 . Let r, Ψ be given by $re^{i\Psi} = z$ then the governing equations in terms of r and Ψ are given by

$$\begin{aligned} \dot{r} &= -r + \frac{K}{2}r(1-r^2) + \frac{F}{2}(1-r^2)\cos(\Psi - u), \\ \dot{\Psi} &= \omega_0 - \frac{F}{2}\left(r + \frac{1}{r}\right)\sin(\Psi - u). \end{aligned} \quad (16)$$

The above equations are used for the wipe-out phase. From the analysis in [CS08] it follows that the system corresponding to r and $\phi := \Psi - ct$ has stable fixed points for certain parameters. Denote a stable fixed point by (r_0, ϕ_0) . As a prediction for u we then take $\Psi - \phi_0$. Note that different from the framework in S2.1 we now have that $\hat{u}(t) := \Psi(t) - \phi_0$. Hence, there is no training phase. During testing, the equations will be given by

$$\begin{aligned} \dot{r} &= -r + \frac{K}{2}r(1-r^2) + \frac{F}{2}(1-r^2)\cos(\phi_0), \\ \dot{\Psi} &= \omega_0 - \frac{F}{2}\left(r + \frac{1}{r}\right)\sin(\phi_0). \end{aligned} \tag{17}$$

Consequently, if the r -equation has a stable fixed point at r_0 then for any $\delta > 0$ and $T_{\text{test}} > 0$ there exists a T_{wipe} such that $|\hat{u}(t) - u(t)| < \delta$ for all $t \in [0, T_{\text{test}}]$. A full analysis of the parameter space can be performed using classical bifurcation theory such as used in [CS08]. It is outside the scope of the Supplementary Information.

In Equation (16) the continuum limit is given for $M = 1$. The techniques in [OA08] can be extended to M -dimensional input. Each input dimension will generate one dependent complex variable in the continuum limit. Hence, if the chaotic input is generated by an autonomous first order ODE the analysis of the system would require the study of (at least) a 6-dimensional first order autonomous ODE.

S5 Supplementary Information to Subsection 2.5

S5.1 Extracting chaos generating maps from the order parameter

When computing the local minima in (Fig. 2c) of the main paper we observed that small fluctuation in r lead to local minima. These anomalies translate to anomalies when we graph consecutive local minima (Fig. S4). However, these can be easily identified by putting bounds on the second derivative which is done to obtain the figure in the main paper.

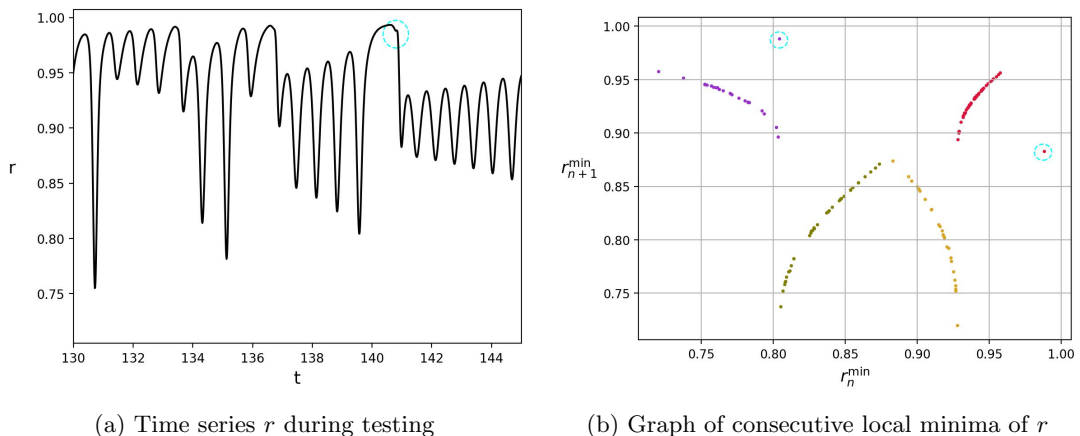


Figure S4: Anomaly in r : We consider r for $t \in [100, 200]$. In terms of local minima there occurs (a) a single local minima which has a small absolute second derivative in comparison to the other local minima, circle in cyan. (b) The anomaly in r translates to two anomalies in the graph corresponding to $r_n^{\min} \mapsto r_{n+1}^{\min}$.

Instead of considering local consecutive minima we can also perform the procedure for consecutive maxima of r . Consider the map $r_n^{\max} \mapsto r_{n+1}^{\max}$. Certain domains for the symbolic mapping are disconnected contrary to the results in the figure of the main paper (Fig. S5a). However, the domains correspond to the same symbolic and attractor dynamics where after an iteration there is a domain that extends to its neighbour on the same wing and a domain that moves to the other wing and covers the full wing (Fig. S5b).

We note that the local maxima of r cover a much smaller range of r compared to local minima of r . Since we wanted to visualize the projection of the critical points on the range of r it was easier to use the local minima.

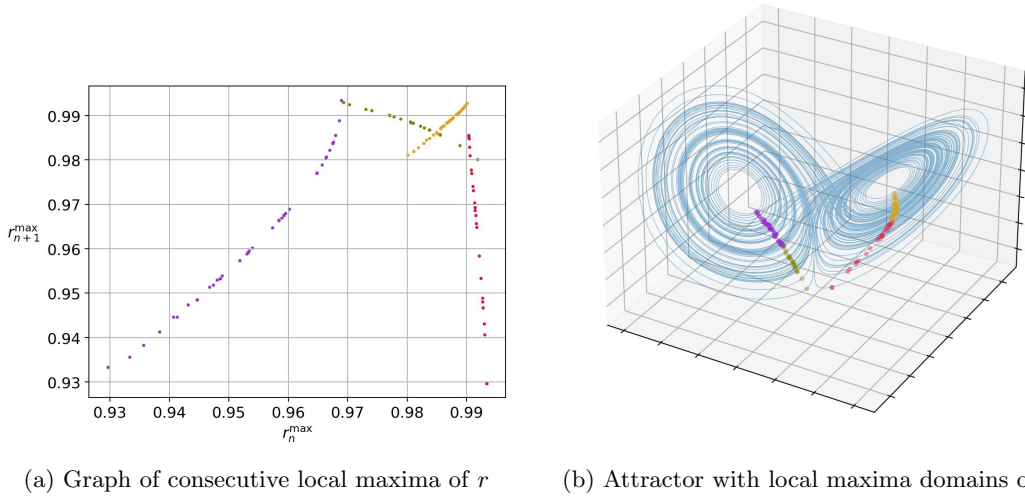


Figure S5: Dynamics of consecutive local maxima of r : By considering the map $r_n^{\max} \mapsto r_{n+1}^{\max}$ we can find a graph that describes the chaotic dynamics of the attractor. Four domains can be identified which on the attractor (b) corresponds to sections which have the characteristic dynamics of the Lorenz system.

S5.2 Dependence of local minima of r on K

Recall the chaotic map considered in the main paper given by $r_n^{\min} \mapsto r_{n+1}^{\min}$. Increasing K leads to a decrease in the range of r^{\min} (Fig. S6). In particular, the global minimum of r appears to be increasing with respect to K .

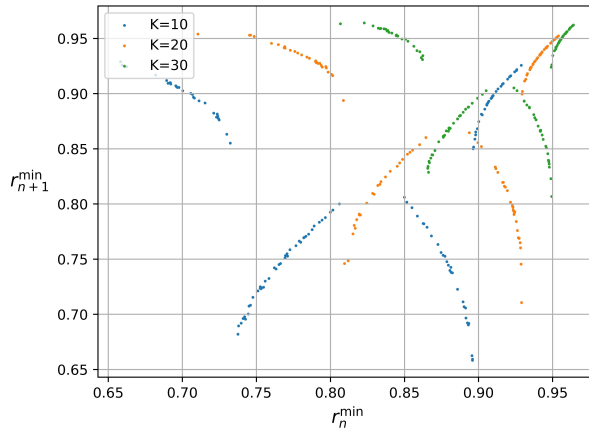


Figure S6: Graph of the map $r_n^{\min} \mapsto r_{n+1}^{\min}$ for varying K and $F = 35$.

S6 Supplementary Information to Subsection 2.6

S6.1 Lyapunov exponents

S6.1.1 Jacobian

The structure of the Kuramoto model allows us to efficiently evaluate the Jacobian. We define $\bar{R}_1(\theta) := \frac{1}{N} \sum_{j=1}^N \sin(\theta_j)$, $\bar{R}_2(\theta) := \frac{1}{N} \sum_{j=1}^N \cos(\theta_j)$. We write the governing equations (1) as

$$\frac{d\theta_i}{dt} = \omega_i + K [\bar{R}_1(\theta) \cos(\theta_i) - \bar{R}_2(\theta) \sin(\theta_i)] + F \sin(c\hat{u}_{v_i}(\theta) - \theta_i). \quad (18)$$

Denote the Jacobian by J . For the closed reservoir $\hat{u}(\theta) = W'[1, \sin(\theta), \sin^2(\theta)]^\top$, $W' \in \mathbb{R}^{M \times (2N+1)}$. We decompose W' as $W' = [W^b, W^1, W^2]$ with $W^b \in \mathbb{R}^{M \times 1}$, $W^1 \in \mathbb{R}^{M \times N}$, $W^2 \in \mathbb{R}^{M \times N}$. Denote the entries of J by $b_{i,j}$ then we have that

$$b_{i,j} = a_{i,j} + cF \cos(c\hat{u}_{v_i}(\theta) - \theta_i) \left(\frac{\partial \hat{u}_{v_i}(\theta)}{\partial \theta_j} \right),$$

with

$$a_{i,j} = \frac{K}{N} \cos(\theta_j - \theta_i) - \delta_{ij} \left(F \cos(\hat{u}_{v_i}(\theta) - \theta_i) + \frac{K}{N} \sum_{k=1}^N \cos(\theta_k - \theta_i) \right),$$

and

$$\frac{\partial(\hat{u})_k(\theta)}{\partial \theta_j} = (W^1)_{k,j} \cos(\theta_j) + 2(W^2)_{k,j} \cos(\theta_j) \sin(\theta_j),$$

for $k = 1, 2, 3, \dots, M$. Note that $a_{i,j} = a_{j,i}$.

S6.1.2 Computation method

The Lyapunov exponents are computed by using the Gram-Schmidt procedure in [PC12, BGG80]. We apply orthonormalization every other step. We used this procedure to compute the largest three Lyapunov exponents of the reservoir. Convergence requires anywhere between 5 to 12 times the training length. This procedure is relatively computationally expensive as evolution of the variational equations has quadratic complexity. The parameter domain in the main paper requires about one week on one CPU. However, this processes can easily be parallelized if you have multiple CPUs available. Additionally, quadratic processes benefit from deployment on GPU.

The fluctuations make it computationally expensive to consider higher order precision. Instead it is better to add a regression step. We can then find parameters for chaotic attractor such that the leading Lyapunov exponent of the reservoir and Lorenz system agree up to three decimals, e.g., $F = 29.719, K = 23.544$.

S6.1.3 Condition attractor climate

Denote the Lyapunov exponents of the Lorenz attractor by $\lambda_j^{\text{Lorenz}}$ with $j = 1, 2, 3$ and let them be arranged in decreasing order. Denote the Lyapunov exponents of the reservoir by λ_j^{res} with $j = 1, 2, \dots, N$ and let them also be arranged in decreasing order. Then, we say that the Lorenz attractor climate is reproduced when $\lambda_i^{\text{Lorenz}} = \lambda_i^{\text{res}}$ for $i = 1, 2$ and $\lambda_k^{\text{res}} < 0$ for $k > 2$ [LHO18]. The numerical condition becomes $|\lambda_i^{\text{Lorenz}} - \lambda_i^{\text{res}}| \leq \epsilon$ for $i = 1, 2$ and $\lambda_k^{\text{res}} \leq -\epsilon$ for $k > 2$, where ϵ us a small positive constant. We say that the attractor type is reproduced when $\lambda_1^{\text{res}} > 0, \lambda_2^{\text{res}} = 0, \lambda_k^{\text{res}} < 0$ for $k > 2$. The numerical condition becomes $\lambda_1^{\text{res}} > \epsilon, |\lambda_2^{\text{res}}| < \epsilon, \lambda_k^{\text{res}} < -\epsilon$. In (Fig. 5b) of the main paper we consider $\epsilon = 0.02$. However, the results for $\epsilon = 0.01$ only differ slightly (Fig. S7).

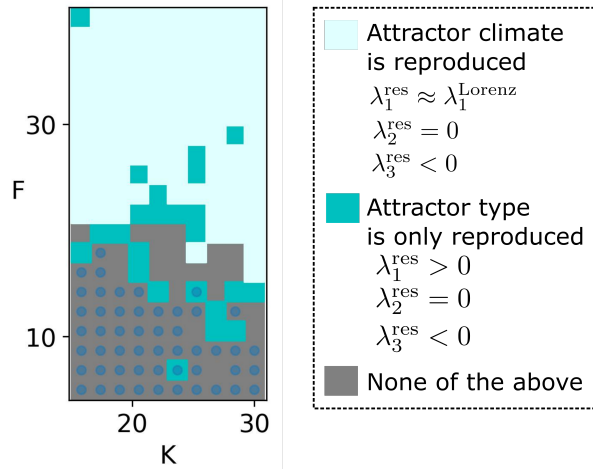


Figure S7: Attractor climate reproduction bifurcation diagrams: Numerical results for $\epsilon = 0.01$

S6.1.4 Lyapunov bifurcation diagram

In (Fig. S8) we consider the sign of the leading three Lyapunov exponents of the reservoir to give more detailed information about the dynamics.

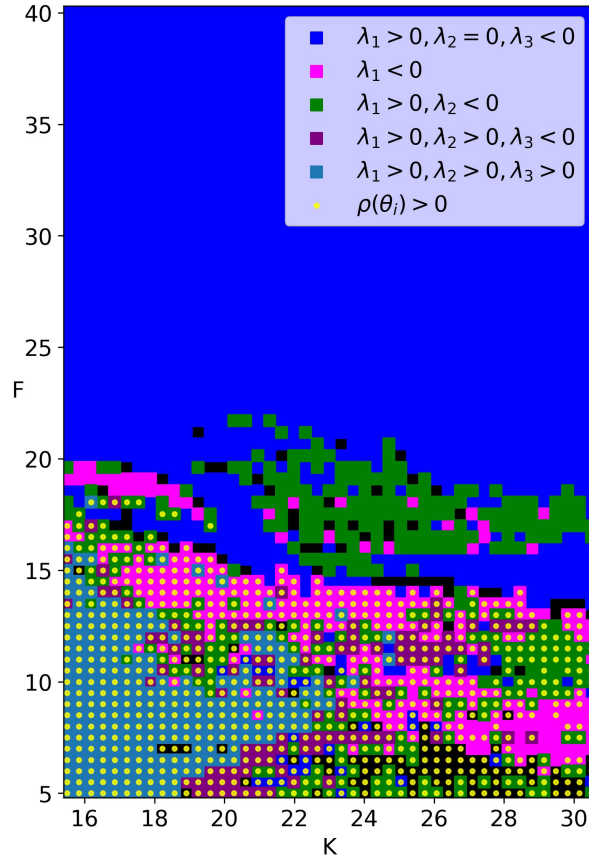


Figure S8: Bifurcation for the leading three Lyapunov exponents: The blue domain corresponds to chaotic attractors which belong to the same family as the Lorenz attractor. The black domain requires higher number of iterations to determine the sign of all the Lyapunov exponents.

Note that because of the compactness of \mathbb{T}^N we do not have that at least one Lyapunov exponent vanishes if the trajectory of an attractor does not contain a fixed point [Hak83].

S6.2 Rotation number

S6.2.1 Numerics

To evaluate the rotation number, $\rho(\theta_k)$, we evaluate the closed reservoir for $2 \cdot 10^4$ time-steps which is equivalent to double of the training length.

S6.2.2 Effect of rotations in the states on the order parameter

In (Fig. S9) we investigate the order parameter r for the case considered in (Fig. 5d) of the main paper. We observe in (Fig. S9a) that r suddenly decreases as full rotations occur. Furthermore, the collectively learned dynamics encoded in the map $r_n^{\min} \mapsto r_{n+1}^{\min}$ also gets lost when the states start making full rotations (Fig. S9b).

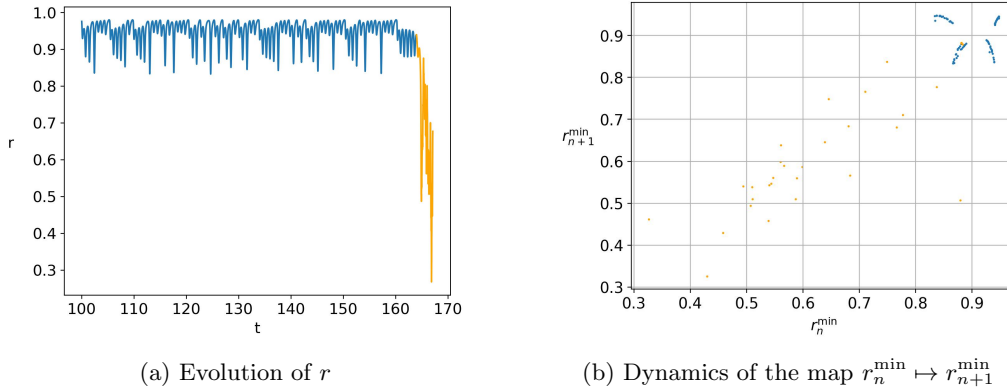


Figure S9: Collapse of the learned dynamics in r : We consider the setting in (Fig. 5d) of the main paper with the same color coding. The r -dynamics collapses which translates to a collapse in the learned chaotic dynamics.

S6.2.3 Continuum limit for constant input

In the continuum limit the average rotations that the oscillators make will be connected to Ψ defined in Section S4.4.2. Let us consider a constant u . Then, for suitable parameters Equation (16) can have a stable limit cycle arising from a Hopf bifurcation [CS08]. These stable limit cycles in a finite-dimensional setting would lead to a diverging rotation number. Note that the rotation number can only diverge for $t \rightarrow \infty$ since the vector field (1) is bounded.

S7 Music box reservoir

The contents of this section concerns the technique behind (Fig. 2d). The task is to memorize and produce sound from a looped piece of sheet music. The sheet music is learned by two reservoir and for each pitch in the sheet music a reservoir is trained that produces the soundwave for that specific pitch. The evolution of the reservoirs is visualized in the accompanying music videos.

S7.1 Learning sheet music

The notes in the sheet music are separated into pitches with a corresponding pitch duration which we refer to as beat. We store these into two separate lists. Below we wrote the lists corresponding to the first bar of the sheet music in (Fig. 2d) of the main paper:

$$\text{pitch list} = [C4, D4, F4, D4, A4, A4, G4, \dots], \quad \text{beat list} = [1/16, 1/16, 1/16, 1/16, 3/16, 3/16, 6/16, \dots].$$

We then stack these lists to arrive at a periodic sequence. Since the Kuramoto reservoir is a continuous reservoir it is difficult to train it on a discrete input. Hence, we first map the values in the lists to unique integers and then apply cubic splines to obtain an interpolation that is used as continuous input for the reservoir (Fig. S10). These periodic continuous inputs are then learned by two separate reservoirs. To retrieve the pitches or beats we sample at the frequency corresponding to the discrete input.

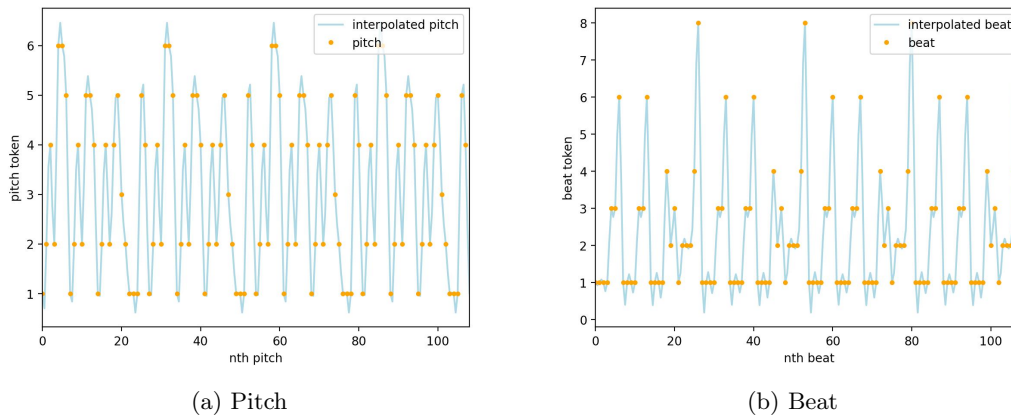


Figure S10: From discrete to continuous input: after mapping pitches and beats to integers we interpolate the discrete data using cubic splines to arrive at a continuous input on which we can train the reservoirs.

S7.2 From pitches to sound

For each pitch in the pitch list we train a sound reservoir which is learned from an instrument soundfile sampled at 22050Hz. Smoothness of the input sound profile is important for the Kuramoto reservoir to learn the input. To see this, observe that if the input is continuous then the vector field corresponding to the Kuramoto reservoir is continuous and hence the prediction must be C^1 -smooth. Organs have very smooth sound profiles. Here, we sampled pitches from a reed organ. A sound profile for an A4 pitch is displayed in (Fig. S11).

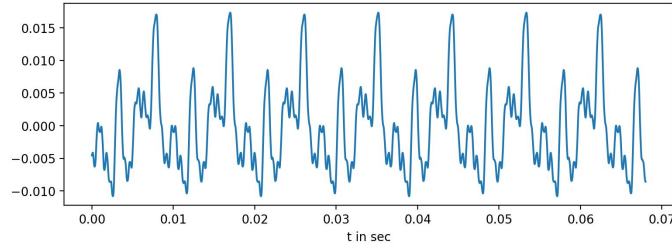


Figure S11: Sound profile of an A4 pitch for a reed organ.

S7.3 Connecting sheet music reservoirs to sound reservoirs

We now put the trained reservoirs together (Fig. S12).

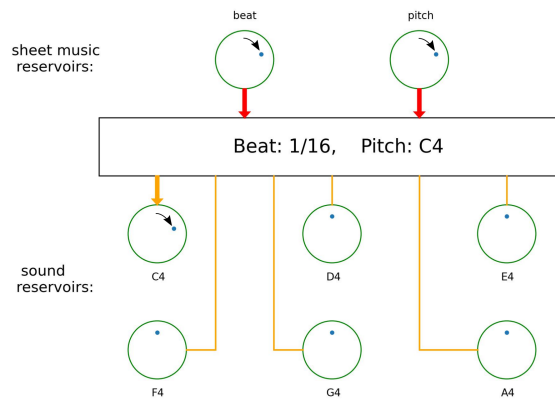


Figure S12: Architecture of the music reservoirs: The beat and pitch reservoirs are evolved to produce a beat and a pitch which initialize the corresponding sound producing pitch reservoir for the duration of the outputted beat.

We evolve the pitch and beat reservoirs which output a pitch with corresponding beat. The outputted pitch initiates the evolution of the corresponding sound producing pitch reservoir for the duration of the outputted beat. The architecture is animated in the accompanying videos.

S8 Rössler system

The Rössler system [Rös76] is given by the ordinary differential equation

$$\begin{aligned}\frac{dx}{dt} &= -y - z, \\ \frac{dy}{dt} &= x + ay, \\ \frac{dz}{dt} &= b + z(x - c).\end{aligned}$$

We consider the parameters $(a, b, c) = (0.2, 0.2, 5.7)$ for which the system has a chaotic attractor.

We repeat the analysis from the main paper for the Rössler attractor (Fig. S13). We observe that the data and the prediction resemble each other in the state space (Fig. S13ab). We investigate the bifurcation

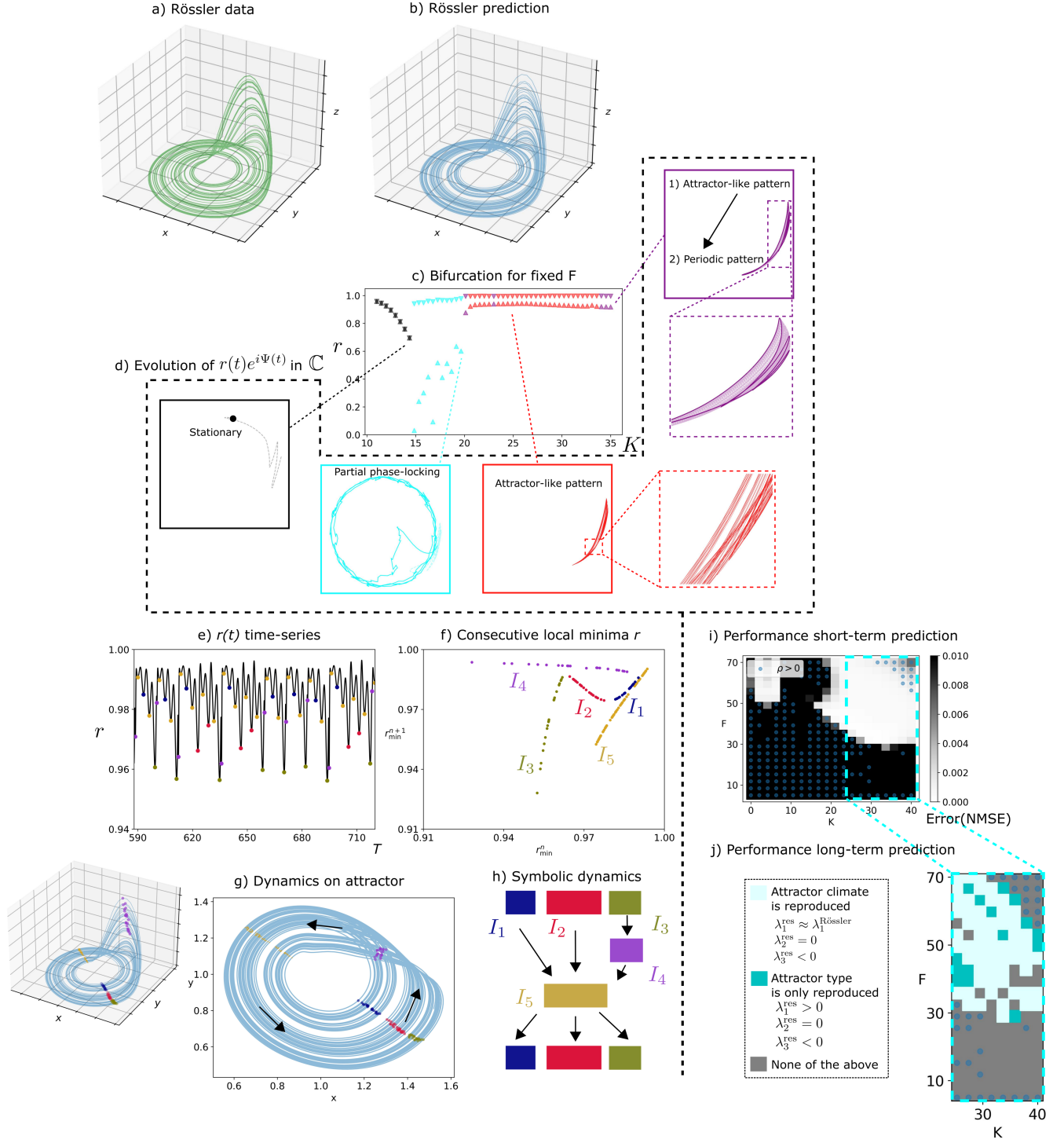


Figure S13: Experiments of the main paper for input time-series on the Rössler attractor.

for fixed F and varying K using the order parameter r (Fig. S13c). This bifurcation is different from the Lorenz case discussed in the main paper. However, it appears to resemble the bifurcation occurring for Lorenz with fixed K and varying F from Section S4.2. In the Rössler system the x, y -components perform a type of rotation and the z -component exhibits spike-like evolution. Hence, the dynamics is different from the Lorenz system and the x, y - and z -dynamics are different. However, the difference in dynamics for x, y -components and z -component of the Rössler can be subdued by applying a suitable rotation matrix to the dependent variables. We observe that for small K the reservoir states become stationary (Fig. S13d). As K is increased partial phase-locking occurs. As K is further increased we arrive at an attractor-like pattern. If K is taken too large periodic motion occurs for the complex order

parameter.

We explore the time-series corresponding to the order parameter r (Fig. S13e). As with the Lorenz system we consider local minima. We visualize consecutive local minima in r and observe that we can identify 5 domains (Fig. S13f). We observe that these domains correspond to a section on the attractor to which we can identify symbolic dynamics (Fig. S13gh).

We consider the NMSE of short-term evolution of the prediction in the K, F -parameter space (Fig. S13i). When F or K is small the error during testing is large. Contrary to the case with the Lorenz system we observe that the error increases when both F and K exceed a threshold. We also include the rotation number ρ . We observe that generally the short-term error is low whenever $\rho = 0$. We investigate if the Rössler attractor's climate is reproduced by comparing the Lyapunov exponents of the reservoir to the Lyapunov exponents of the Rössler attractor (Fig. S13j). Above an F the parameters for which the climate is reproduced are abundant. However, if K is too large the prediction exhibits periodic behaviour and the climate is not reproduced.

We note that the leading Lyapunov exponent of the Rössler attractor is much smaller than the leading Lyapunov exponent of the Lorenz attractor: $\lambda_1^{\text{Lorenz}} \approx 0.91$, $\lambda_1^{\text{Rössler}} \approx 0.07$. Hence, we would expect that the embedded attractor for the Rössler system is more parameter-sensitive than the embedded attractor for the Lorenz system.